Development and validation of evaporation model for a multi-component fuel considering volume-average internal mass and enthalpy

Yushin Naito, Nozomu Hashimoto, Osamu Fujita

Department of Engineering, Hokkaido University, Nishi 8 Kita13, Kita-ku, Sapporo, Hokkaido, Japan

Highlights

- A droplet evaporation model was developed for multi-component fuel.
- Internal distributions of the mass fraction and the enthalpy were developed.
- Internal distributions are satisfying the conservation of mass and enthalpy.
- The predicted results are in good agreement with the experimental results.
- Internal distributions have a major impact on the results at practical conditions.

Nomenclature

C_p	Heat capacity, J/mol/K
D	Diffusion coefficient, m^2/s
D_{eff}	Effective diffusion coefficient defined by Eq.(19), m^2/s
h	Sensible enthalpy for Eq.(22), J/kg
H_{latent}	Latent heat, J/kg
k	Thermal conductivity, W/(m K)
k_{eff}	Effective thermal conductivity defined by Eq.(20), W/(m K)
m	Mass of droplet, kg
MW	Molecular weight, g/mol
$\dot{m}$	Mass evaporation rate, kg/s
N	Number of chemical species in gas phase
N_l	Number of chemical species in liquid phase
P	Pressure, Pa
$\dot{q}$	Heat energy, W
R	Distance from the droplet center, m
R_d	Droplet diameter, m
Δt	Time step, s
T	Temperature, K
u	Velocity, m/s
u^c	The modified Stephan velocity, m/s
v	Diffusion velocity, m/s
x	Mole fraction
y	Mass fraction

Subscripts:

a	Average
amb	Ambient
c	Critical
g	Gas
i	i species
l	Liquid
m	Mixture system
ref	Reference value
s	Surface
v	Vapor

Greek symbols:

ε	Normalized mass fraction
η	Viscosity, kg/m/s
ρ	Density, kg/m^3
σ	Stefan-Boltzmann constant (5.67×10^{-9}), $W/m^2/K^4$
Ω	Dimensionless temperature

Abstract

We developed a droplet evaporation model for a multi-component fuel, considering the nonuniform distributions of both mass fraction and temperature inside multi-component fuel droplet. The distribution equations satisfy the conservation of droplet mass and enthalpy. We proposed mass fraction and temperature distribution equations inside a droplet to accurately determine variations between the numerical assumptions of a liquid phase and a gas phase. We found that an obvious gradient appears in the mass fraction and temperature distribution profiles at various ambient temperatures. To verify the accuracy of the developed model, we further compared the predicted droplet lifetimes with the experimental results at various ambient temperatures. The consideration of the pre-evaporation process led to more accurate droplet lifetime prediction using the present model. We also investigated the differences between the present model and the uniform distribution model. The difference in the predicted droplet lifetime becomes more than 10% at practical spray combustion conditions. Thus, internal distribution of mass fraction ad temperature must be considered in practical spray combustion simulations.

Keywords: Droplet evaporation; Multi-component fuel; Internal distribution; Numerical model; Spray combustion

1. Introduction

Computational fluid dynamics (CFD) provides remarkable advantages for the prediction of combustion characteristics in a combustion chamber. Many researchers have performed CFD studies to clarify the characteristics of complex spray flames encountered in combustor design. Especially, the droplet evaporation process is an important

parameter in the design of spray combustors. Nomura *et al*. [1] investigated the droplet evaporation characteristics in subcritical and supercritical environments. Moriai *et al*. [2] revealed the differences between the predicted and the measured droplet diameters in a subscale aircraft jet engine combustor. They found that the selection of the droplet evaporation model affects the differences between the predicted and measured droplet diameters. Furthermore, Noh *et al.* [3] compared the droplet evaporation models for a turbulent non-swirling jet flame and found that different droplet evaporation models predicted the different locations of lifted flame and droplet distributions. Thus, the accuracy of the droplet evaporation model may affect the prediction of the spray flame structure. A high-precision droplet evaporation model can help to optimize spray combustor design.

For a precise simulation of the practical spray combustion field, droplet evaporation models for multi-component fuel, such as practical fuel, have been developed. Some researchers have suggested droplet evaporation models considering uniform internal distributions [4-7]. However, the formation of gradient distributions for both concentration and temperature inside a droplet is expected because of various fuel volatility in multi-component droplet evaporation. Some droplet evaporation models assuming unsteady diffusion inside the droplet have also been developed [8,9]. Torres *et al.* [9] suggested the droplet evaporation model for multi-component fuels using interior discretization, which is used in engine CFD codes. Although the one-dimensional model can provide precise evaporation information, the discretization method for droplets comprising large numbers of chemical species requires an unrealistic central processing unit time. To decrease the calculation cost, a continuous thermodynamic model (CTM) has been developed to analyze droplet evaporation for multi-component fuels by using a

continuous function of either the normal boiling temperature or molecular weight [10,11]. Despite the improved computational efficiency, however, CTMs cannot calculate the evaporation rate of each fuel species.

The droplet evaporation model for multi-component fuels considering the internal distributions for mass fraction and temperature has been developed without using numerical grids. Yi *et al.* [12] have suggested the droplet evaporation model considering the internal distributions of mass and temperature inside a droplet. Their model approximated the mass and temperature distributions inside a droplet by a quadratic polynomial function. As a theoretical model for multi-component droplet evaporation, Sazhin *et al.* suggested various models on the basis of the discrete multi-component (DMC) approach. Their droplet evaporation model introduces the mass fraction and temperature distributions inside a droplet as a function of two variables which are the length from droplet center and time. The equations are given by the analytical solutions of a stationary spherically symmetric multi-component droplet. The model takes into account droplet heating by convection from the ambient gas, the distribution of temperature and diffusion of liquid species inside the droplet [13,14]. Furthermore, they suggested a new multi-dimensional quasi-discrete model in terms of heating and evaporation of Diesel fuel. This model takes into account the contribution of various groups of hydrocarbons in Diesel fuels and quasi-components are formed within individual groups [15]. The difference in the predicted evaporation times between the multi-component and single component models has been also investigated for f biodiesel, Diesel and gasoline droplet heating and evaporation [16]. Recently, a new model for puffing and micro-explosions in water-fuel emulsion droplets is suggested [17]. However, their droplet evaporation models have not satisfy the mass and enthalpy conservation

inside the droplet in overall droplet evaporation process even though the conservation of mass and energy inside droplet have been satisfied in each time step. This is because quasi-steady-state mass and enthalpy diffusions were assumed in the gas phase, whereas the diffusions of mass and enthalpy in unsteady states were considered in the liquid phase. In a quasi-steady state, the amount of diffused mass from the droplet is overestimated compared with that in an unsteady state. Hence, the differences in the numerical simulation assumption for the liquid and gas phase may result from the violation of conservation. Furthermore, the effect of the droplet evaporation on the gas phase is ignored in their model.

In this study, we developed a droplet evaporation model for multi-component fuels, which can satisfy the conservation of mass and enthalpy inside the droplet and is intended for spray combustion simulations. We derived the internal distributions of mass and enthalpy which can simulate mass and enthalpy conservation during the droplet evaporation process. To satisfy the conservation of mass and enthalpy, the volume-average internal mass and enthalpy expressed by $y_{i,l}^{a}\int_0^{R_d} 4\pi R^2\, dR = \int_0^{R_d} y_{i,l}(t,R)4\pi R^2\, dR$ and $T^a \int_0^{R_d} 4\pi C_{p,l} R^2\, dR = \int_0^{R_d} T(R,t)4\pi C_{p,l} R^2\, dR$ were applied to the distribution equations. To consider the coexistence of the unsteady state along with the quasi-steady state, mass fraction distribution, which has a boundary between the gradient and uniform distribution, was introduced. Furthermore, the present model take account for the effect of gases on droplet without considering the coupling and the concept of region between the droplet and gas. Finally, the accuracy of the developed model was verified at various ambient temperatures in comparison with experimental results. In [15], the model was applied to bi-component fuel (ethanol and acetone) when ambient

temperature is room temperature. Even though the accuracy of the model is not verified at high ambient temperature in [15], the accuracy of the present model is verified at both low and high ambient temperature.

2. Numerical Model

2.1 General description of the numerical model

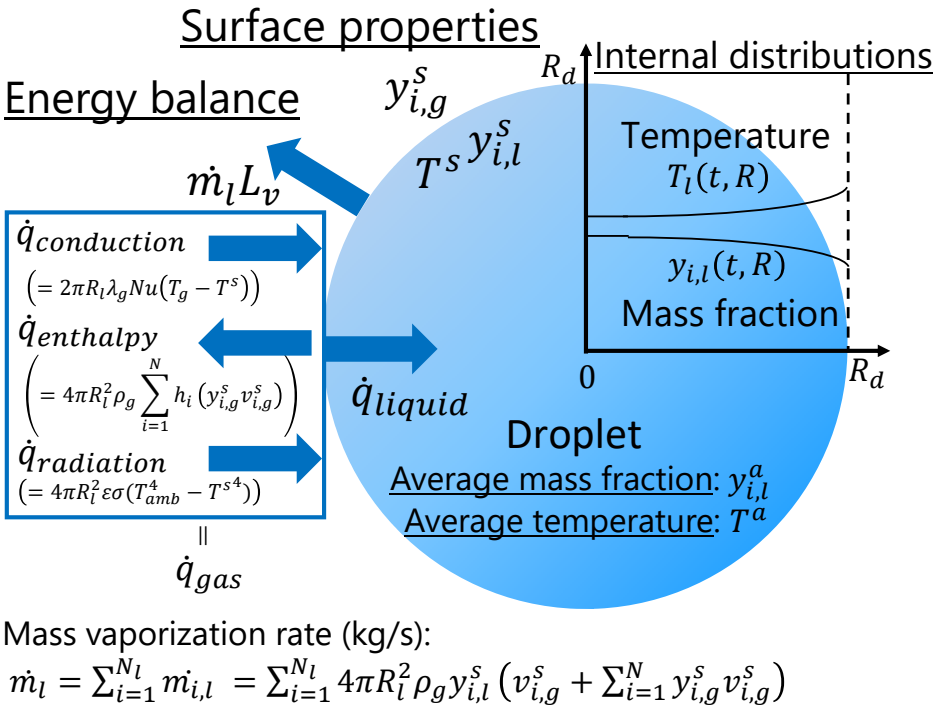

Fig. 1. Schematic of the droplet evaporation model for multi-component fuel.

Figure 1 shows the schematic of our droplet evaporation model for multi-component fuels. In the liquid phase, we consider the mass fraction distribution, $y_{i,l}(t,R)$, and the temperature distribution, $T_l(R,t)$, inside a droplet, which are given by the analytical solutions of a partial differential equation with spherical coordinates. The average mass fraction of each species ($y_{i,l}^a$) is given by the mass balance of each species and updated every timestep. The average temperature is also given by the energy conservation inside

the droplet. There is no need to consider the coupling of heat and mass transfer in the present model. This is because the heat transfer and mass transfer are separately considered in both liquid and gas phase. According to the mass transfer in the gas phase, the present model applies the mass diffusion in multi-component system as the mass evaporation rate of multi-component fuel of each species. The heat transfer is assumed as the quasi-steady diffusion in the gas phase. In preset model, not only the effect of heat transfer from the gas phase to the droplet but also the effect of heat transfer from the droplet to the gas phase are considered. The enthalpy from the gas phase to the liquid phase ($\dot{q}_{gas}$) comprises three terms, the heat conduction from the gas phase ($\dot{q}_{conduction}$), the enthalpy diffusion from the liquid phase ($\dot{q}_{enthalpy}$), and the radiation from the gas phase ($\dot{q}_{radiation}$). The mass evaporation rate of each species ($\dot{m}_{i,l}$) is given by the multi-component system analysis of the equation of continuity. At the droplet interface, the energy balance, $\dot{q}_{liquid} = \dot{q}_{gas} - \sum_{i=1}^{N_l} \dot{m}_{i,l} H_{i,latent}$, is considered. In the present model, we assumed that (1) the fuel droplet is spherically symmetric, (2) Dufour and Soret effects are neglected, (3) the droplet interface follows the thermodynamic equilibrium, and (4) the gas-phase follow the quasi-steady-state assumption. Note that the dimensionless number and thermodynamic properties used in the present model are described in Appendix A-C.

2.2 Liquid phase

2.2.1 Diffusion of species inside a droplet

We assume that part of the droplet has a uniform species distribution to improve the

accuracy of modeling the mass diffusion. This is because there is a possibility that the mass does not diffuse completely from the droplet surface to the droplet center during a short time step, especially when the ambient temperature is high such as practical combustion field. Figure 2 shows the distribution of the mass concentration of each species in the uniform-gradient domain. The boundary x between the uniform distribution ($\varphi_{i,l}(t,R)$) and the gradient distribution ($\psi_{i,l}(t,R)$) is defined by the mass diffusion distance from the droplet surface. The mass diffusion distance is determined by the ratio of the effective mass diffusion coefficient $D_{eff,i}$ and the radius regression rate $\dot{R}_d$. Thus, the boundary is given by $x = R_d - \max\{D_{eff,i} | i \in N_l\}/\dot{R}_d$. The fuel species mass diffusion inside a spherically symmetric droplet can be expressed by the following equation:

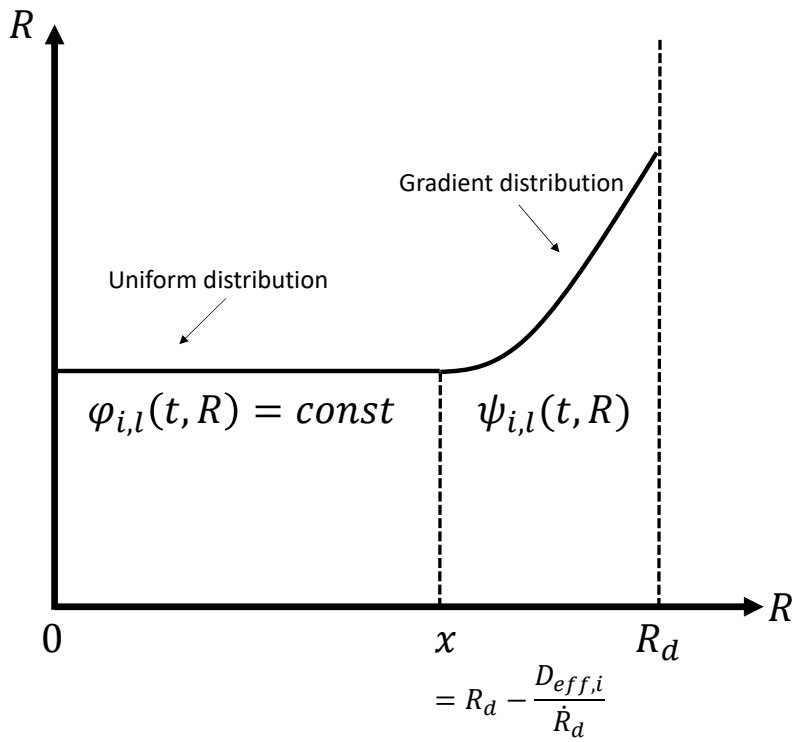

Fig. 2. Diagram showing the boundary x between the uniform distribution ($\varphi_{i,l}(t,R)$) and the gradient distribution ($\psi_{i,l}(t,R)$).

$$\frac{\partial y_{i,l}}{\partial t} = D_{eff,i}\left(\frac{\partial^2 y_{i,l}}{\partial R^2} + \frac{2}{R}\frac{\partial y_{i,l}}{\partial R}\right) \tag{1}$$

Sazhin *et al.* [14,16] previously suggested an analytical solution for Eq. (1) with the boundary conditions at the droplet center and surface. In our model, the boundary conditions based on the two-layer concepts shown in Fig.2 is described as

$$\begin{aligned} &\frac{\dot{m}_l}{4\pi\rho_l R_d^2}\left(\varepsilon_i - y_{i,l}^s\right) = -D_{eff,i}\frac{\partial y_{i,l}}{\partial R} && (R = R_d) \\ &\frac{\partial y_{i,l}}{\partial R} = 0 && (R = 0) \\ &y_{i,l}(t, x^-) = y_{i,l}(t, x^+), \left.\frac{\partial y_{i,l}}{\partial R}\right|_{R=x^+} = \left.\frac{\partial y_{i,l}}{\partial R}\right|_{R=x^-} = 0 \end{aligned} \tag{2}$$

where ε_i is the normalized fuel vapor fraction, defined as $\varepsilon_i = y_{i,g}^s / \sum_{i=1}^{N_l} y_{i,g}^s$. The analytical solution of Eq. (1) with the boundary conditions given by Eq. (2) can be described as

$$\begin{aligned} Y_{i,l}(t,R) = \varepsilon_i(t) + \frac{1}{R}\Bigg\{&\exp\left[D_{eff,i}\left(\frac{\lambda_0}{R_d}\right)^2 t\right]\left[q_{i,n} - \varepsilon_i(0)\mathrm{Q}_0\right]\sinh\left(\lambda_0\frac{R}{R_d}\right) \\ &+ \sum_{n=1}^{\infty}\exp\left[-D_{eff,i}\left(\frac{\lambda_n}{R_d}\right)^2 t\right]\left[q_{i,n} - \varepsilon_i(0)\mathrm{Q}_n\right]\sin\left(\lambda_n\frac{R}{R_d}\right)\Bigg\} \end{aligned} \tag{3}$$

where $h_0 = -\left(1 + \frac{\dot{m}_l}{4\pi\rho_l R_d^2}\frac{R_d}{D_{eff,i}}\right)$ and

$$Q_n = \begin{cases} \dfrac{1}{\|v_0(R)\|^2}\left(\dfrac{R_d}{\lambda_0}\right)^2\{\lambda_0\cosh(\lambda_0) - \sinh(\lambda_0)\} & (\text{when } n = 0) \\ \dfrac{1}{\|v_n(R)\|^2}\left(\dfrac{R_d}{\lambda_n}\right)^2\{\sin(\lambda_n) - \lambda_n\cos(\lambda_n)\} & (\text{when } n \geqq 1) \end{cases}$$

$$q_{i,n} = \begin{cases} \dfrac{1}{\|v_0(R)\|^2} \begin{cases} \displaystyle\int_0^x R\varphi v_0(R)dR & \text{(when } 0 < R < x) \\ \displaystyle\int_x^{R_d} R\psi_{i,l0}(0,R)v_n(R)dR & \text{(when } x < R < R_d) \end{cases} & (n = 0) \\ \dfrac{1}{\|v_n(R)\|^2} \begin{cases} \displaystyle\int_0^x R\varphi v_n(R)dR & \text{(when } 0 < R < x) \\ \displaystyle\int_x^{R_d} R\psi_{i,l0}(0,R)v_n(R)dR & \text{(when } x < R < R_d) \end{cases} & (n \geqq 1) \end{cases}$$

Next, the derivation processes of the eigenvalues λ_0 and λ_n ($n \geqq 1$) are described. The following boundary conditions are given in the present study, instead of Eq. (52) in Ref. [14]:

$$\begin{cases} v|_{R=0} = \left(\dfrac{\partial v}{\partial R} + \dfrac{h_0}{R_d}v\right)_{R=R_d} = 0 \\ v|_{R=x^-} = v|_{R=x^+} \\ D_{eff,i}[x\dfrac{\partial v}{\partial R} - v]\Big|_{R=x^+} = 0 \end{cases} \tag{4}$$

When $p < 0$ in the Eq.(51) in Ref. [14], we can write the general solution assuming that $p = -\lambda^2 < 0$ as

$$v(R) = Acosh\left(\lambda\frac{R}{R_d}\right) + Bsinh\left(\lambda\frac{R}{R_d}\right)$$

where A and B are arbitrary constants. The boundary conditions obtained using Eq. (4) lead to the following equations:

$$\begin{cases} v(0) = A\cosh\left(\lambda\dfrac{0}{R_d}\right) + B\sinh\left(\lambda\dfrac{0}{R_d}\right) = A = 0 \\ \left(\dfrac{\partial v}{\partial R} + \dfrac{h_0}{R_d}v\right)_{R=R_d} = \dfrac{B}{R_d}(\lambda\cosh(\lambda) + h_0\sinh(\lambda)) = 0 \\ D_{eff,i}[x\dfrac{\partial v}{\partial R} - v]\Big|_{R=x^+} = B\left(\dfrac{\lambda}{R_d}x\cosh\left(\lambda\dfrac{x}{R_d}\right) - \sinh\left(\lambda\dfrac{x}{R_d}\right)\right) = 0 \end{cases} \tag{5}$$

B in this equation is not equal to 0 because the present study does not assume a trivial solution where $v = 0$. Thus, Eq. (5) can be rearranged as

$$\lambda\cosh(\lambda) + h_0 \sinh(\lambda) - \lambda x\cosh\left(\lambda\frac{x}{R_d}\right) + R_d\sinh\left(\lambda\frac{x}{R_d}\right) = 0 \tag{6}$$

Then, the solution of Eq. (6) gives only one eigenvalue $\lambda = \lambda_0 > 0$ and the corresponding eigenfunction.

$$v_0(R) = \sinh\left(\lambda_0\frac{R}{R_d}\right)$$

where the normalization leading to $B = 1$ is chosen. Furthermore, the direct calculation of the integrals leads to the following description for the norm of the eigenfunction v_0.

$$\|v_0\|^2 = \int_0^{R_d} v_0^2(R)\, dR = \frac{R_d}{4\lambda_0}(\sinh(2\lambda_0) - 2\lambda_0)$$

Furthermore, when p > 0 in Eq. (51) in Ref. [14], we can write the general solution assuming that $p = \lambda^2 > 0$ as

$$v(R) = A\cos\left(\lambda\frac{R}{R_d}\right) + B\sin\left(\lambda\frac{R}{R_d}\right)$$

where A and B are arbitrary constants. The boundary conditions obtained using Eq. (4) lead to the following equations:

$$\begin{aligned} v(0) &= A\cos\left(\lambda\frac{0}{R_d}\right) + B\sin\left(\lambda\frac{0}{R_d}\right) = A = 0 \\ v(R_d) &= \frac{B}{R_d}(\lambda\cos(\lambda) + h_0\sin(\lambda)) = 0 \\ D_{eff,i}[x\frac{\partial v}{\partial R} - v]\Big|_{R=x^+} &= B\left(\frac{\lambda}{R_d}x\cos\left(\lambda\frac{x}{R_d}\right) - \sin\left(\lambda\frac{x}{R_d}\right)\right) = 0 \end{aligned} \tag{7}$$

B in this equation is not equal to 0 because the present study does not consider the trivial solution $v = 0$. Therefore, Eq. (7) can be rearranged as

$$\lambda\cos(\lambda) + h_0 \sin(\lambda) - \lambda x\cos\left(\lambda\frac{x}{R_d}\right) + R_d\sin\left(\lambda\frac{x}{R_d}\right) = 0 \tag{8}$$

Then, the solution of Eq. (8) gives a countable set of positive solutions λ_n which are arranged in ascending order such as $0 < \lambda_1 < \lambda_2 < \lambda_3 < \cdots$, and the corresponding eigenfunction can be described as

$$v_n(R) = \sin\left(\lambda_n\frac{R}{R_d}\right)$$

where the normalization leading to $B = 1$ is chosen. Furthermore, the direct calculation of the integrals leads to the following description for the norm of the eigenfunction v_n.

$$\|v_n\|^2 = \int_0^{R_d} v_n^2(R)\, dR = \frac{R_d}{\lambda_n}\left\{\frac{\lambda_n}{2} - \frac{1}{4}\sin(2\lambda_n)\right\}$$

The analytical solution given by Eq. (3) is uniquely determined in mathematics. However, the disadvantage of using the analytical solution in numerical simulations is that it necessitates interactive calculation (e.g., Ref. [18]), which increase the calculation cost. Thus, the variables can be assumed constant during a short time step, which has been applied in numerical studies using the analytical solution [13].

In this study, we assumed that ε_i is constant during the short time step and used the distributions obtained at the previous time step, which are described as $\psi_i(t,R)$ and $\varphi_i(t,R)$. Assuming that ε_i, $\psi_i(t,R)$, and $\varphi_i(t,R)$ are constant during the short time step, the authors deform Eq. (3) to satisfy mass conservation inside the droplet as the follows:

$$y_{i,l}^a \int_0^{R_d} 4\pi R^2\, dR = \int_0^{R_d} y_{i,l}(t,R) 4\pi R^2\, dR \tag{9}$$

Note that the calculation for $y_{i,l}^a$ is introduced in Section 2.4. Eq. (9) has not been reported

in Sazhin's former studies (e.g. Ref. [16]). Substituting Eq. (3) into Eq. (9), we obtained the following identical equation:

$$\frac{1}{3}y_{i,l}^{a}R_d^3 = \frac{1}{3}\varepsilon_{i,l}R_d^3 + A_0\left\{\frac{R_d^2}{\lambda_0}cosh(\lambda_0) - \left(\frac{R_d}{\lambda_0}\right)^2 sinh(\lambda_0)\right\} + \sum_{n=1}^{\infty} A_n\left\{-\frac{R_d^2}{\lambda_n}cos(\lambda_n) + \left(\frac{R_d}{\lambda_n}\right)^2 sin(\lambda_n)\right\} \tag{10}$$

where $A_0 = exp\left[D_{i,l}\left(\frac{\lambda_0}{R_d}\right)^2 t\right]\left[q_{i0} - \varepsilon_{i,l}(0)Q_0\right]$, and $A_n = exp\left[-D_{i,l}\left(\frac{\lambda_n}{R_d}\right)^2 t\right]\left[q_{in} - \varepsilon_{i,l}(0)Q_n\right]$. Eq. (10) can be rearranged as

$$\varepsilon_{i,l} = y_{i,l}^{a} - \frac{3A_0}{R_d\lambda_0^2}\{\lambda_0\, cosh(\lambda_0) - sinh(\lambda_0)\} - \sum_{n=1}^{\infty}\frac{3A_n}{R_d\lambda_n^2}\{sin(\lambda_n) - \lambda_n\, cos(\lambda_n)\} \tag{11}$$

Equation (11) has no variable because ε_i is constant during the short time step. By substituting Eq. (11) into Eq. (9), the distribution equation of each fuel species can be given by

$$y_{i,l}(t,R) = y_{i,l}^{a} + \frac{1}{R}\left[exp\left[D_{eff,i}\left(\frac{\lambda_0}{R_d}\right)^2 t\right](q_{i0} - \varepsilon_i Q_0)\left\{sinh\left(\lambda_0\frac{R}{R_d}\right) - \frac{3R}{R_d\lambda_0^2}(\lambda_0\, cosh(\lambda_0) - sinh(\lambda_0))\right\} + \sum_{n=1}^{\infty} exp\left[-D_{eff,i}\left(\frac{\lambda_n}{R_d}\right)^2 t\right][q_{in} - \varepsilon_i Q_n]\left\{sin\left(\lambda_n\frac{R}{R_d}\right) - \frac{3R}{R_d\lambda_n^2}(sin(\lambda_n) - \lambda_n\, cos(\lambda_n))\right\}\right] \tag{12}$$

2.2.2 Droplet heating

According to former study [19], it has been pointed out that the thermal diffusivity is much larger than the mass diffusivity inside droplet in conventional hydrocarbon fuels. This leads that the temperature is easier to form a distribution along the whole droplet

than the mass concentration inside droplet. This is why we focused on the precise theory of the mass diffusion inside droplet in the present model. The heat transfer inside a spherically symmetric droplet can be expressed by the following equation:

$$C_{p,l}\rho_l \frac{\partial T}{\partial t} = k_{eff}\left(\frac{\partial^2 T}{\partial R^2} + \frac{2}{R}\frac{\partial T}{\partial R}\right) \tag{13}$$

The boundary conditions at the center and surface of the droplet can be described as:

$$\begin{aligned} 2\pi R_d k_g Nu(T_{amb} - T^s) - \dot{q}_{enthalpy} + \dot{q}_{radiation} - \dot{m}_l H_{latent} &= k_{eff}\frac{\partial T}{\partial R} \quad (R = R_d) \\ \frac{\partial T}{\partial R} &= 0 \quad (R = 0) \end{aligned} \tag{14}$$

Some conventional models (e.g. [16]) have not considered the enthalpy diffusion term. However, the enthalpy diffusion flux in a multi-component energy balance is well-known, yet it is a frequently neglected term [20]. Furthermore, our previous study [21] clarified that the consideration of the enthalpy diffusion term results in a slower evaporation rate. On the basis of Refs. [16] and [18], the solution of Eq. (13) with the boundary conditions (Eq. (14)) can be given by

$$T(t,R) = \frac{R_d}{R}\sum_{n=1}^{\infty} q_n\, exp[-\kappa\lambda_n^2 t]\, sin\left(\lambda_n \frac{R}{R_d}\right) + T_{eff} \tag{15}$$

where $\kappa = \frac{k_{eff}}{C_{p,l}\rho_l R_d^2}$, $\|v_n\|^2 = \frac{1}{2}\left[1 + \frac{H}{H^2+\lambda_n^2}\right]$, $H = \frac{k_g Nu}{2k_l} - 1$, $T_{eff} = T_{amb} + \frac{1}{2\pi R_d k_g Nu}\left(-\dot{q}_{enthalpy} + \dot{q}_{radiation} - \dot{m}_l H_{latent}\right)$, and

$q_n = \frac{1}{R_d^2 \|v_n\|^2} \int_0^{R_d} R T_0(R) \, sin\left(\lambda_n \frac{R}{R_d}\right) dR - \frac{(1+H)T_{eff}}{\lambda_n^2 \|v_n\|^2} sin(\lambda_n)$. Note that T_{eff} is a function of time because $\dot{m}_l$ and T_{amb} are time-dependent. The estimation of $C_{p,l}$ and ρ_l is described in Appendix A. The estimation of k_g and is described in Appendix B.

Assuming that T_{eff} and $T_0(R)$ are constant during a short time step, as in Ref. [18] , and $T_0(R)$ is obtained at the previous time step, the authors deform Eq. (15) to satisfy enthalpy conservation inside the droplet as the following:

$$T^a \int_0^{R_d} 4\pi C_{p,l} R^2 \, dR = \int_0^{R_d} T(R,t) 4\pi C_{p,l} R^2 \, dR \tag{16}$$

We assumed that the heat capacity inside the droplet ($C_{p,l}$) is constant, although heat capacity is a function of temperature. Substituting Eq. (15) into Eq. (16), we obtain the following identical equation:

$$\frac{4}{3}\pi T^a = 4\pi \left\{ -\sum_{n=1}^{\infty} \frac{q_n \, exp[-\kappa \lambda_n^2 t]}{\lambda_n} cos(\lambda_n) + \sum_{n=1}^{\infty} \frac{q_n \, exp[-\kappa \lambda_n^2 t]}{\lambda_n^2} sin(\lambda_n) \right\} + \frac{4}{3}\pi T_{eff} \tag{17}$$

Similar to the derivation process of the mass distribution equation, the temperature distribution equation can be given by

$$T(t,R) = T^a + \sum_{n=1}^{\infty} q_n \, exp[-\kappa \lambda_n^2 t] \left\{ \frac{R_d}{R} sin\left(\lambda_n \frac{R}{R_d}\right) - 3 \frac{(1+H) \, sin(\lambda_n)}{\lambda_n^2} \right\} \tag{18}$$

To consider effect of internal circulation caused by the internal vortex on the droplet evaporation characteristics, the effective mass diffusivity (D_{eff}) [22] and the effective thermal diffusivity (k_{eff}) [23] were applied, instead of the normal mass diffusivity and the normal thermal diffusivity as

$$D_{eff,i} = \left\{1.86 + 0.86\, tanh\left[2.225\, log_{10}\left(\frac{Re_l Sc_l}{30}\right)\right]\right\} D_{l,i} \tag{19}$$

$$k_{eff} = \left\{1.86 + 0.86\, tanh\left[2.225\, log_{10}\left(\frac{Pe_l}{30}\right)\right]\right\} k_l \tag{20}$$

Note that the effective mass and thermal diffusivity have been applied to some droplet evaporation model for multi-component fuel (e.g. [13]) without using a detailed and analytical approach such as [24]. The estimation of $D_{l,i}$ and k_l is described in Appendix A.

2.3 Gas-phase

2.3.1 Mass evaporation rate

In this study, the mass evaporation rate ($\dot{m}_l$) for each fuel species was expressed on the basis of the continuity equation for fuel vapor at the droplet surface in ambient gas. According to Ref. [25], the total mass evaporation and the mass evaporation of species *i* in quiescent conditions were given by

$$\dot{m}_l = \sum_{i=1}^{N_l} \dot{m}_{i,l} = \sum_{i=1}^{N_l} 4\pi R_d^2 \rho_g^s y_{i,g}^s (v_{i,g}^s - \sum_{i=1}^{N} y_{i,g}^s v_{i,g}^s) \tag{21}$$

The estimation of ρ_g and is described in Appendix B.

2.3.2 Heat transfer

Three distinct terms were considered when analyzing the gas-phase heat flux: the heat flux of conduction from the gas phase to the liquid phase ($\dot{q}_{conduction}$), that of enthalpy diffusion from the liquid phase to the gas phase ($\dot{q}_{enthalpy}$), and that of heat radiation from the phase to the liquid phase ($\dot{q}_{radiation}$). Although the enthalpy diffusion flux in a multi-component energy balance is well-known, it is a frequently neglected [20]. However, our previous study using internal distribution formulas approximated by the quadratic polynomial functions [21] elucidated that the consideration of the enthalpy diffusion term reduces the evaporation rate. Moreover, the evaporation model calculation results agreed better with the experimental results when the enthalpy diffusion term was considered [21]. Thus, the total heat flux from the gas phase can be described as

$$\begin{aligned}\dot{q}_{gas} &= \dot{q}_{conduction} + \dot{q}_{enthalpy} + \dot{q}_{radiation} \\ &= 2\pi R_d k_g Nu(T_{amb} - T^s) - 4\pi R_d^2 \rho_g \sum_{i=1}^{N} h_{i,g}\left(y_{i,g}^s v_{i,g}^s\right) + 4\pi R_d^2 \varepsilon\sigma(T_{amb}^4 - T^{s4})\end{aligned} \tag{22}$$

Note that dimensionless numbers used in this work are summarized in Appendix C. The estimation of ρ_g and $h_{i,g}$ is described in Appendix B.

2.4 Gas–liquid interface

2.4.1 Thermodynamic equilibrium

On the basis of Raoult's law, the vapor mole fraction at the droplet surface ($x_{i,g}^{s}$) was calculated as

$$x_{i,g}^{s} = \frac{P_{i,v}}{P_{amb}} x_{i,l}^{s} \tag{23}$$

where $x_{i,l}^{s}$ is the liquid mole fraction at the droplet surface, P_{amb} is the ambient pressure [Pa], and $P_{i,v}$ is the vapor pressure of species *i* [Pa] calculated using the Antoine equation as

$$log_{10} P_{i,v} = A_{i,p} - \frac{B_{i,p}}{C_{i,p} + T^{s}} \tag{24}$$

where $A_{i,p}$, $B_{i,p}$, and $C_{i,p}$ are Antoine constants [26].

2.4.2 Energy equilibrium

The energy balance at the gas–liquid interface can be expressed as

$$\dot{q}_{gas} - \dot{q}_{liquid} = \sum_{i=1}^{N_l} \dot{m}_{i,l} H_{i,latent} \tag{25}$$

2.4.3 Energy and mass conservations within a droplet

The average temperature inside the droplet (T^{a}) at the *n*th time step can be calculated from the governing equation for energy in the liquid phase as

$$C_{p,l} m_l \frac{dT^a}{dt} = \dot{q}_{liquid} \Leftrightarrow T_{n+1}^a = T_n^a + \frac{\dot{q}_{liquid}}{C_{p,l} m_l} \Delta t \tag{26}$$

The droplet radius (R_d) [m] was calculated on the basis of the droplet mass at each time step.

$$R_d = \left(\frac{m_l - \dot{m}_l \Delta t}{\frac{4}{3} \pi \rho_l} \right)^{\frac{1}{3}} \tag{27}$$

Moreover, the average mass fraction of species *i* inside the droplet ($y_{i,l}^a$) [–] was calculated on the basis of the droplet mass and mass evaporation rate as

$$y_{i,l}^a = \frac{m_{i,l} - \dot{m}_{i,l} \Delta t}{m_l - \dot{m}_l \Delta t} \tag{28}$$

2.6 Numerical algorithm

The calculation code of the present model was developed using Fortran 90. Figure 3 shows the numerical algorithm of the present model. The calculation procedure can be described as follows:

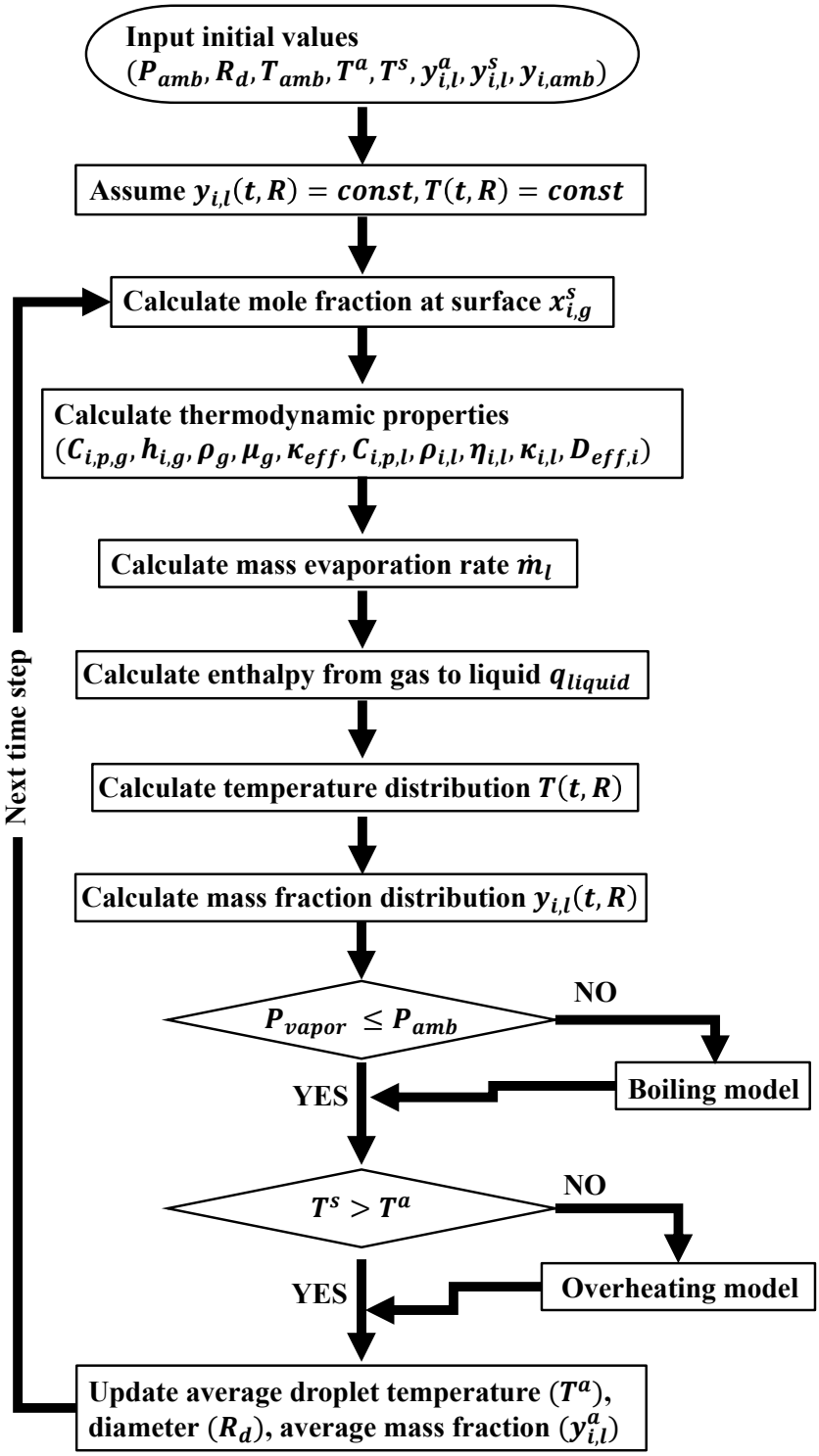

Fig.3 Numerical algorithm of present model

1. Input the initial values ($P_{amb}, T_{amb}, R_d, T^a, T^s$, and $y_{i,l}^a$).
2. Assume uniform temperature and mass fraction distributions inside the droplet at the initial step, or use the distributions from the previous time step.
3. Calculate thermodynamic equilibrium at the gas–liquid interface given by Eq. (23).
4. Calculate thermodynamic properties in liquid and gas phases.
5. Calculate the mass evaporation rate given by Eq. (21).
6. Calculate the energy balance at the droplet interface given by Eq. (25).
7. Calculate the droplet temperature distribution given by Eq. (12).
8. Calculate mass fraction distributions inside the droplet given by Eq. (18).
9. Update average droplet temperature (T^a) given by Eq. (26), the droplet diameter (R_d) given by Eq. (27), and average mass fraction of species i ($y_{i,l}^a$) given by Eq. (28). Repeat steps 2-9 until the droplet total mass becomes 0.

Note that the explanations for the boiling model and the overheating model are described in Appendix D and E, respectively. In the conditions shown in Section 3.2, the total vapor pressure does not exceed the ambient pressure. In other word, the droplet temperature does not exceed the temperature equivalent to boiling point. The droplet average temperature given by Eq. (26) also does not exceed the surface temperature in the conditions shown in Section 3.2. This is why the both the boiling model and the overheating model were not activated. On the other hand, both the boiling model and the overheating model were activated in the conditions shown in Section 3.3. However, the

boiling model and the overheating model had little effect on the prediction results because the boiling model and the overheating model were used very infrequently in calculations.

2.7 Surrogate fuel

For the validation of the present model, a surrogate fuel for light cycle oil (LCO) [27] was used as a multi-component fuel, which includes eicosane ($C_{20}H_{42}$), n-hexadecane ($C_{16}H_{34}$), 1-methylnaphthalene ($C_{11}H_{10}$), and tert-butylbenzene ($C_{10}H_{14}$) with initial mass fractions of 0.0729, 0.1753, 0.4402, and 0.3116, respectively. We found that the evaporation characteristics of this surrogate fuel were in good agreement with those of the actual LCO.

3. Results and Discussion

3.1 Internal distributions

We investigated the internal distribution behavior of the involved species as a function of ambient temperature (T_{amb}) first. To reproduce the experimental conditions [27], the initial droplet diameter (D_0) was selected as 500 μm, nitrogen was used as the ambient gas, and the ambient pressure was 0.1 MPa. Fig. 4 shows the history of the internal mass distribution of each fuel species as a function of the nondimensional length from droplet center to the surface during evaporation at T_{amb} = 473 K. In this figure, the color shows the mass fraction, and the horizontal distributions describe the mass fraction distribution at each moment. According to Fig. 4, the gradients of the mass fraction distributions of all fuel species were found in the early evaporation stage. Fig. 5 shows the internal distributions as a function of normalized length from the droplet center to the surface at

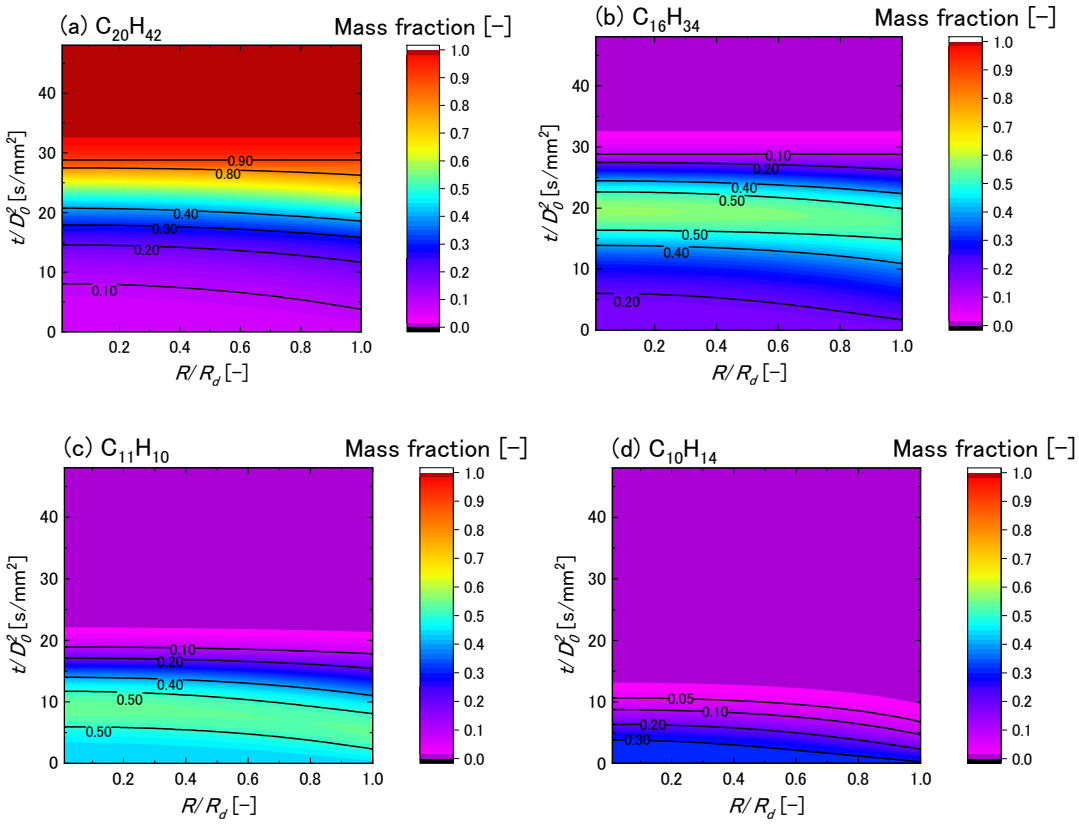

Fig. 4. History of internal mass distributions of each fuel species as a function of the nondimensional length from the droplet center to the surface during evaporation at T_{amb} = 473 K.

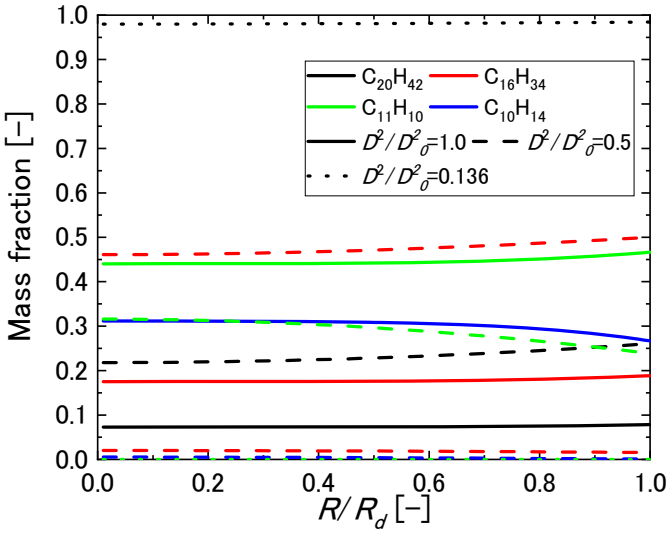

Fig. 5. Internal mass fraction distribution of each fuel species as a function of normalized length from the droplet center to the surface at early (D^2/D_0^2 = 1.0), middle (D^2/D_0^2 = 0.5), and late evaporation terms (D^2/D_0^2 = 0.136) at T_{amb} = 473 K

397

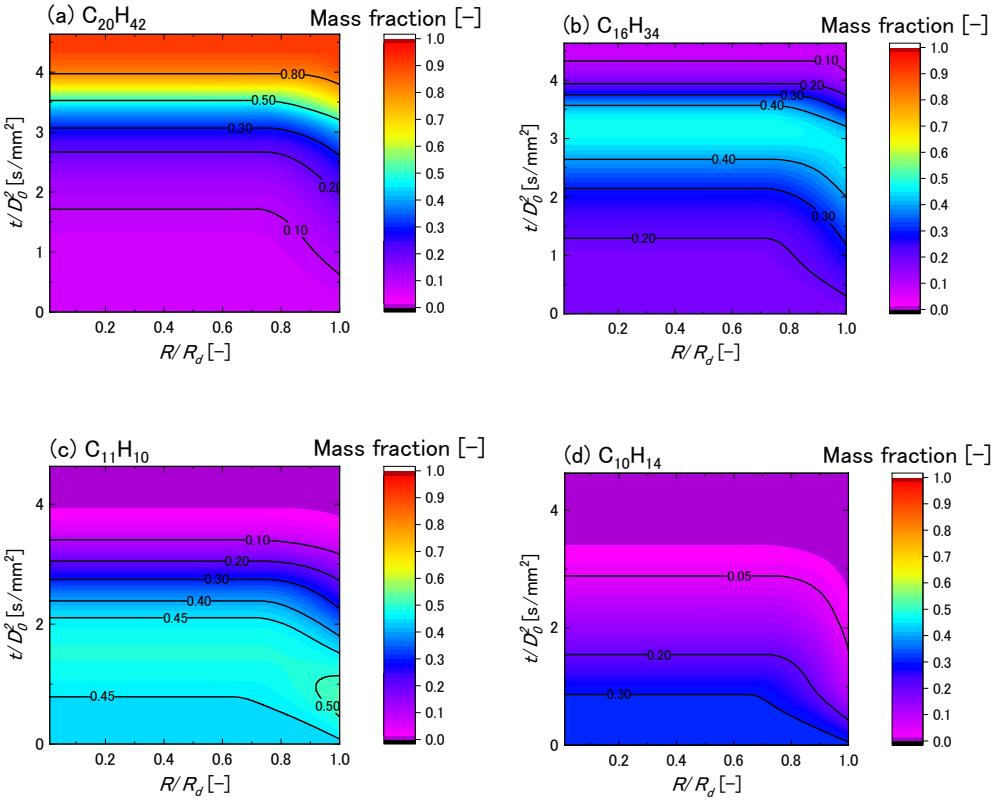

Fig. 6. History of internal mass distributions of each fuel species as a function of the nondimensional length from the droplet center to the surface during evaporation at T_{amb} = 873 K

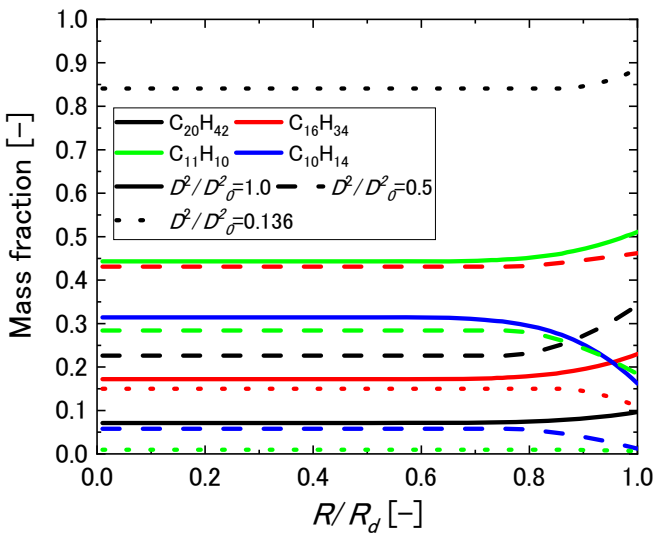

Fig. 7. Internal mass fraction distributions of each fuel species as a function of normalized length from the droplet center to the surface at early (D^2/D_0^2 = 1.0), middle (D^2/D_0^2 = 0.5), and late evaporation term (D^2/D_0^2 = 0.136 at T_{amb}= 873 K

early (D^2/D_0^2 = 1.0), middle (D^2/D_0^2 = 0.5), and late evaporation term (D^2/D_0^2 = 0.136) at T_{amb} = 473 K. At the early evaporation term, the gradients of mass distribution for the highly volatile species, $C_{11}H_{10}$ and $C_{10}H_{14}$, decrease, whereas those with low volatility, $C_{16}H_{34}$ and $C_{20}H_{42}$, increase toward the droplet surface because the highly volatile species evaporate more rapidly from the droplet surface than those with low volatility species. However, the gradients of all fuel species become close to constant over time. At the late evaporation term, the mass fraction distributions of $C_{16}H_{34}$ and $C_{20}H_{42}$ become almost constant and $C_{20}H_{42}$ is dominant inside the droplet, including the effect of considering internal mass fraction distributions is remarkable in the early evaporation stage at a relatively low ambient temperature. A detailed discussion about the effects of internal distributions on the evaporation behavior is provided in Section 3.3.

In the case of T_{amb} = 873 K, Fig. 6 shows more remarkable gradient distributions of all fuel species during the whole evaporation term than Fig. 4 (T_{amb} = 473 K). As for the case of T_{amb} = 473 K, Fig. 7 shows the internal distributions as a function of normalized length from the droplet center to the surface at T_{amb} = 873 K. According to Fig. 7, the gradients of mass distributions for all species around the droplet surface are steeper than those in Fig.5. Then, the gradient becomes flat over time. Hence, the effect of considering the gradient inside the droplet becomes larger as the ambient temperature increase.

Figure 8 shows the internal temperature distributions as a function of the nondimensional length from the droplet center to the surface during evaporation at (a) T_{amb} = 473 and (b) 873 K. According to Fig. 8-(a), the internal temperature distribution becomes almost constant during the evaporation term. However, comparing Fig. 8-(b) with Fig. 8-(a), we found that the internal temperature gradient becomes steeper in higher ambient temperature as shown in Fig.8-(b). Thus, the consideration of temperature

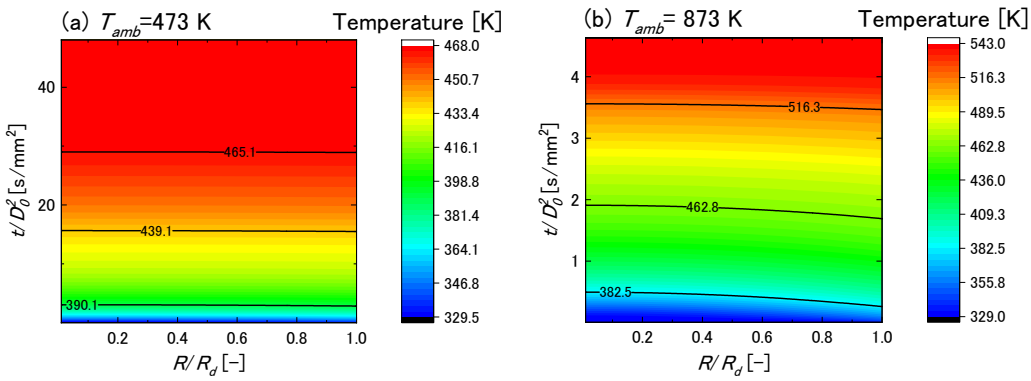

Fig. 8. Temperature distributions inside the droplet at (a) T_{amb} = 473 and (b) 873 K.

distribution inside a droplet plays an important role in the modeling of droplet evaporation for a multi-component fuel at high ambient temperatures.

3.2 Evaluation of model accuracy

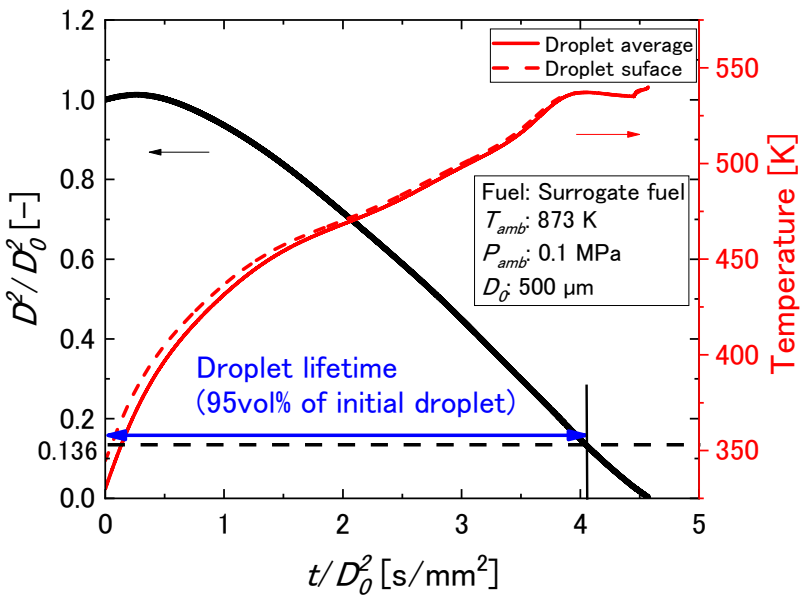

Fig. 9. Predicted droplet diameter and temperature.

Figure 9 depicts the history of the squared droplet diameter and the droplet average and surface temperatures as functions of time, normalized by the squared initial droplet

diameter. The conditions used were T_{amb} = 873 K and P_{amb} = 0.1 MPa, with a 500 μm initial droplet diameter (D_0) to reproduce the experimental conditions [27]. As demonstrated in Fig. 9, the developed model reproduced the droplet diameter increase due to thermal expansion diameter in the early evaporation period, which was also found in the experimental results [28]. The droplet lifetime is the normalized time required for the evaporation of 95% of the initial droplet volume (D^2/D_0^2 = 0.136) [29]. Meanwhile, Fig. 9 demonstrates differences between the droplet surface temperature and average temperature. We present the detailed results obtained by the developed model and verify its accuracy in the following sections.

Figure 10 shows the predicted droplet lifetime for every 10 K from T_{amb} = 473 to 873 K and the experimental results at various ambient temperature [28] to verify the accuracy of the present model. In Fig.10, the plots of experimental data indicate the average droplet lifetime of three or more experiments, and the maximum and minimum value of error bar are the maximum and minimum value of three or more experiments, respectively. Before

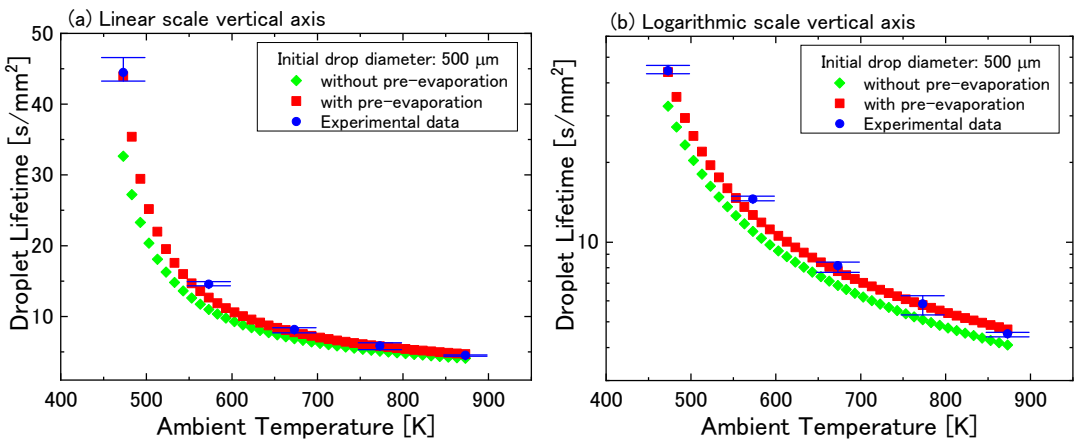

Fig. 10. Comparison between measured [28] and calculated droplet lifetimes at various ambient temperatures given by (a) linear scale in vertical axis and (b) logarithmic scale in vertical axis.

the detailed results are described, the meaning of pre-evaporation presented in Fig. 11 is explained as follows. Figure 11 depicts the experimental process of pre-evaporation. First, the fuel droplet was generated by a droplet generator on the tip of a droplet suspender (Fig. 11(a)). At that time, the surrounding gas temperature was 323 –353 K. Simultaneously, the fuel droplet, with a diameter in the range of 500 μm ±15% was suspended at the intersection point of two fibers (Fig. 11(b)). Evaporation could begin soon after the droplet was suspended. The ambient gas was kept at 323 – 333 K (Fig. 11(c)). The pre-evaporation occurred in the process shown in Fig. 11(c). Finally, the suspended droplet was inserted into the hot chamber, in which ambient temperatures were in the range of 473 –873 K, to record the droplet evaporation behavior using a high-speed camera (Fig. 11(d)). As Fig. 10 indicates, the calculated results without pre-evaporation differ from the experimental results at various ambient temperatures. Particularly, the

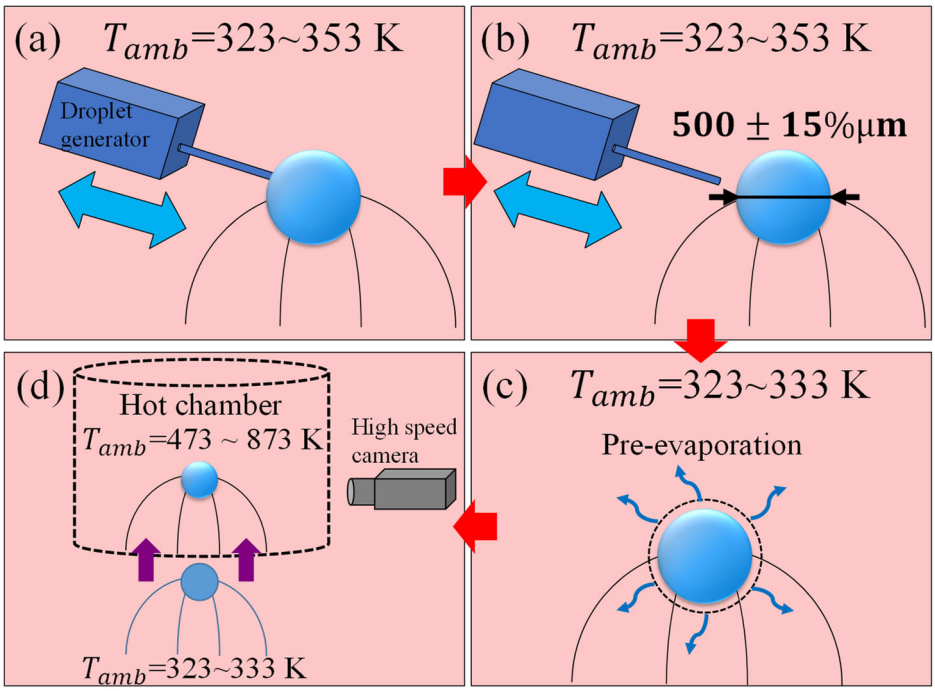

Fig. 11. Schematic of pre-evaporation process in experiments.

largest difference between the calculated and experimental results are found at T_{amb} = 473 K. The differences between the calculated and experimental results may be caused by a change in the initial mass fractions of the surrogate fuel in the experiments due to the pre-evaporation. According to Fig.10(a), there are obvious differences between measured and predicted droplet lifetime without considering pre-evaporation term at T_{amb} = 473 K.

To increase the accuracy of the developed numerical model, this study also simulated pre-evaporation. The initial values for pre-evaporation term and main-evaporation term are shown in Table 1. In the calculation, the fuel droplet was assumed to remain at 330 K for 60 s before the droplet was inserted into a hotter chamber. Note that the initial droplet diameter in the calculation was set at 515 μm because the initial diameter before the pre-evaporation stage in the experiment was expected to be larger than the measured diameter in the hot chamber. Fig. 10 shows the comparison between measured and predicted droplet lifetime considering pre-evaporation term at various ambient temperature. According to Fig.10(a), the predicted droplet lifetime considering pre-evaporation term is in better agreement with the experimental results than the predicted droplet lifetime ignoring pre-evaporation term in low ambient temperature. Furthermore, it is found that the predicted droplet lifetime considering pre-evaporation term is in better agreement

Table 1 Initial values for pre-evaporation term and main-evaporation term

		Pre-evaporation term	Main-evaporation term
Ambient temperature	[K]	330	473 ~ 873
Ambient pressure	[MPa]	0.1	0.1
Droplet radius	[μm]	515	Value at end of pre-evaporation term
Droplet temperature	[K]	330	Value at end of pre-evaporation term
Ambient gas	[-]	N_2	N_2

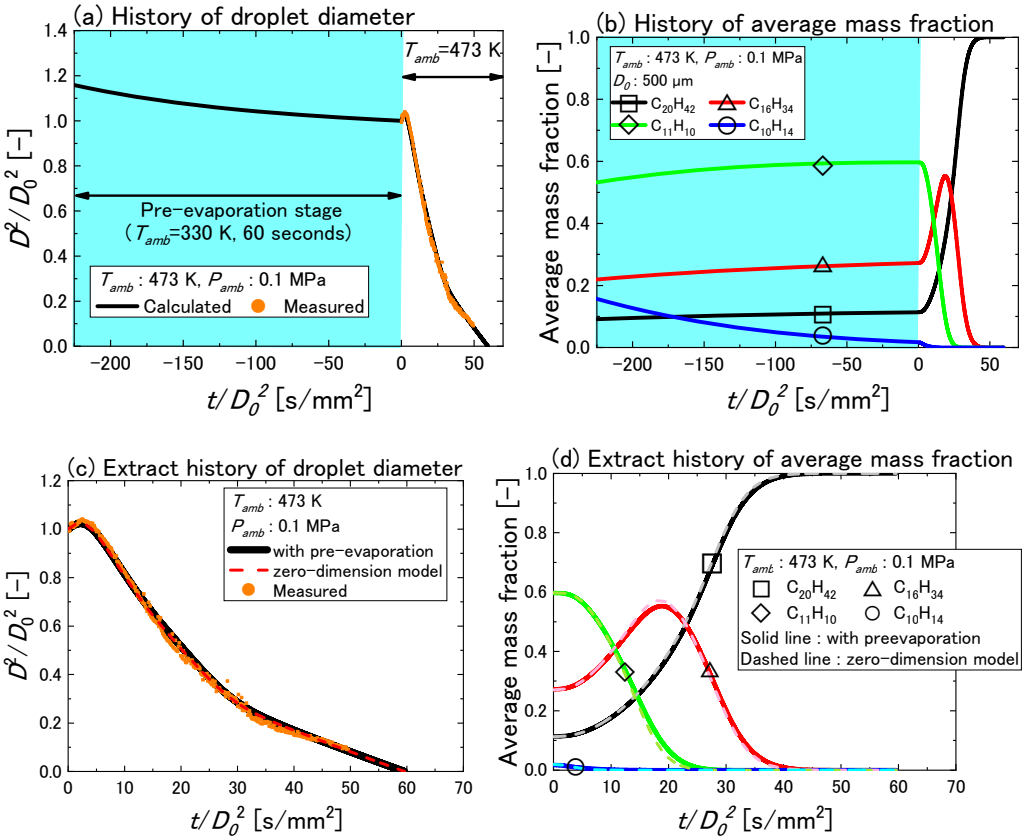

Fig. 12. Comparison between the experimental results and the simulated results considering the pre-evaporation process for (a) the history of the normalized squared droplet diameter, (b) the history of the average mass fraction of each species inside droplet, (c) extracted history of the normalized squared droplet diameter, and (d) extracted history of the average mass fraction of each species inside droplet at $T_{amb} = 473\ K$.

with the experimental results than the predicted droplet lifetime ignoring pre-evaporation term in high ambient temperature as shown in Fig10(b). Figure-12(a) shows the history of the normalized square of the droplet diameter as a function of normalized time at T_{amb} = 473 K. During the pre-evaporation stage, the normalized square of the droplet diameter gently decreases. The predicted results of history of the normalized square of the droplet diameter are in good agreement with the experimental result. Figure 12(b) shows the average mass fraction values inside the droplet as a function of normalized

time. As seen in the pre-evaporation stage in Fig. 12(b), the species with the highest volatility, $C_{10}H_{14}$, almost entirely evaporated before the droplet was inserted into the hot chamber. To precisely compare the history of the normalized square of the droplet diameter between the predicted results and measured results, the plots in Fig. 12(a) are extracted as shown in Fig. 12(c). Furthermore, the history of the normalized square of the droplet diameter predicted by the present model is compared with that predicted by the zero-dimension model. Note that the zero-dimensional model is defined as the model that has uniform temperature and mass fraction distribution in this paper. The plots in Fig. 12(b) are also extracted as shown in Fig. 12(d). In Fig. 12(d), the history of average mass fraction predicted by the present model is compared with that predicted by the zero-dimension model. According to both Fig. 12(c) and Fig. 12(d), there are few differences in the history of predicted results between the present model and zero-dimension model. However, it is found that there are clear differences between the present model and zero-dimension model at practical spray combustion conditions. The detailed information will be discussed in Section 3.3. Finally, the predicted droplet lifetimes considering pre-evaporation are compared with the measured droplet lifetimes at various ambient temperatures in Fig. 10. Table 2 shows the concrete value of both measured and predicted

Table 2 Differences in droplet lifetime between measurements and predictions at various ambient temperature

Ambient temperature [K]	Measurement [s/m^2]	Prediction ignoring pre-evaporation term [s/m^2]	Difference [%]	Prediction considering pre-evaporation term [s/m^2]	Difference [%]
473	44.480	32.652	36.225	43.977	1.145
573	14.561	10.992	32.472	12.661	15.010
673	8.151	6.860	18.816	7.768	4.929
773	5.843	5.092	14.745	5.783	1.043
873	4.503	4.088	10.156	4.681	-3.806

droplet lifetime and the differences in predicted droplet lifetime from measurements at various ambient temperatures. It is found that differences decreased when considering pre-evaporation term compared to when not considering pre-evaporation term in all ambient temperature.

3.3 Effect of internal distributions at spray combustion conditions

We investigated the effect of considering the internal temperature and mass concentration distributions inside the droplet. In previous section, we defined the zero-dimensional model. The zero-dimensional model has uniform temperature and mass fraction distribution. To elucidate the effect of considering the internal temperature and mass concentration distributions inside the droplet, the zero-dimensional model was compared with the present model. Furthermore, for the future use of the present model in practical spray combustion simulations, smaller initial droplet diameters were investigated. In this section, 60 and 20 μm were selected as initial droplet diameters on the basis of former experimental [30-32] and simulation studies [2]. To evaluate the effect of considering internal distributions quantitatively, the differences in predicted droplet diameter between the present model and the model assuming that internal distributions both temperature and mass concentrations are uniform. Figure 13 shows the

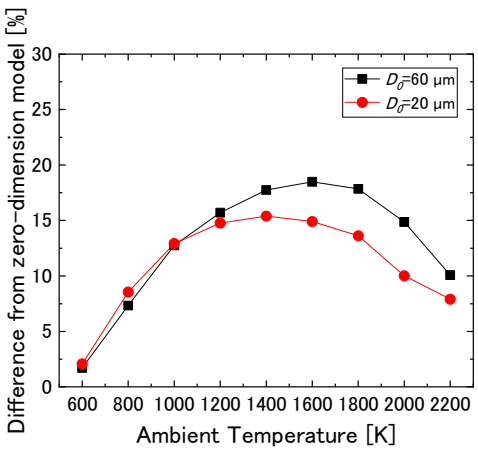

Fig. 13 Droplet lifetime differences between present model and zero-dimension model under various ambient temperature

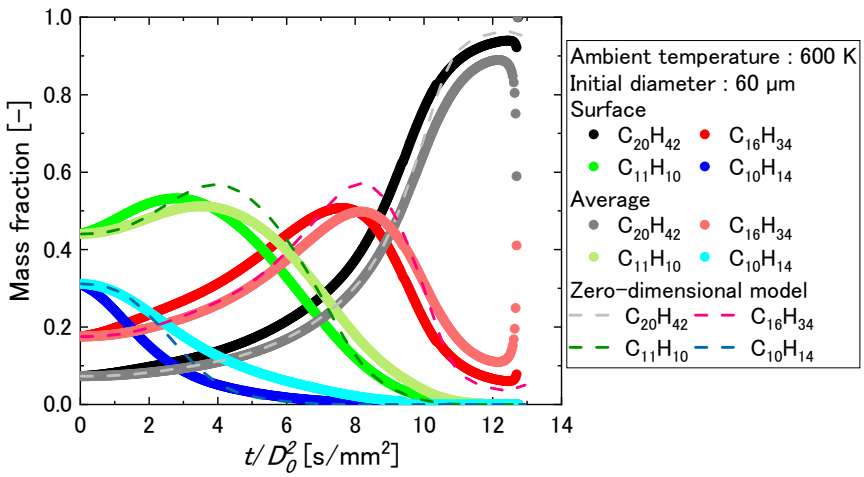

(a) History of liquid mass fraction

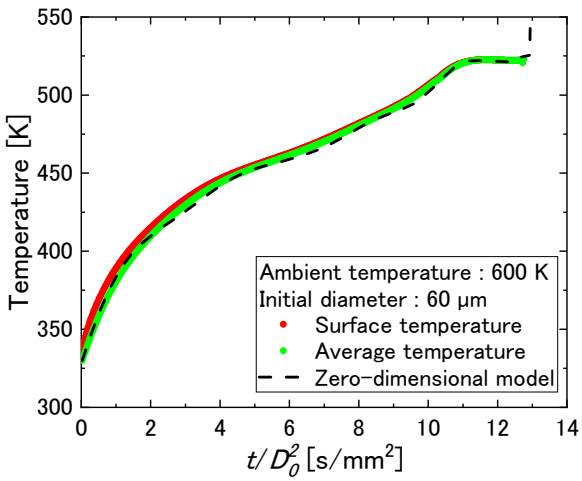

(b) History of droplet temperature

Fig.14 Comparison of the predicted results between the present model and the zero-dimensional model for (a) mass fraction and (b) temperature inside droplet at T_{amb}=600 K in D_0=60 μm.

comparison of the differences in droplet lifetimes formed by the present model and the zero-dimensional model at various ambient temperatures, which include both experimental and practical ambient temperatures. The divergence from the zero-dimensional model increases with the increased ambient temperature for both initial droplet diameters. Figure 14 shows the comparison of the predicted results between the

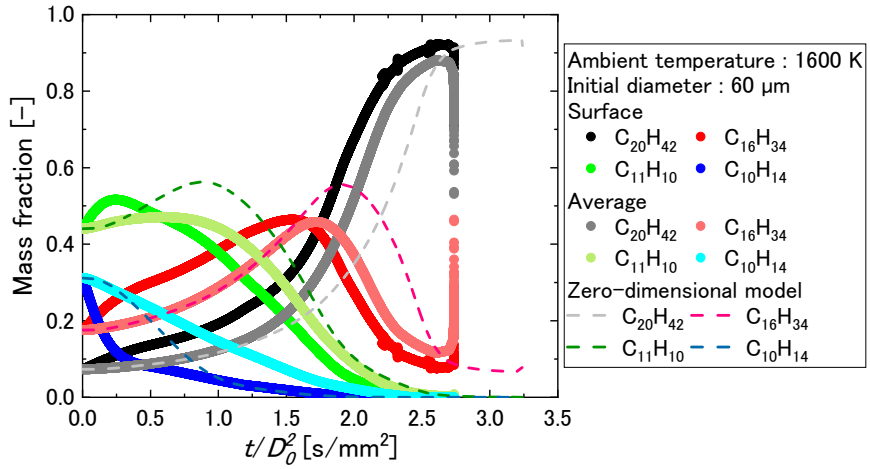

(a) History of liquid mass fraction

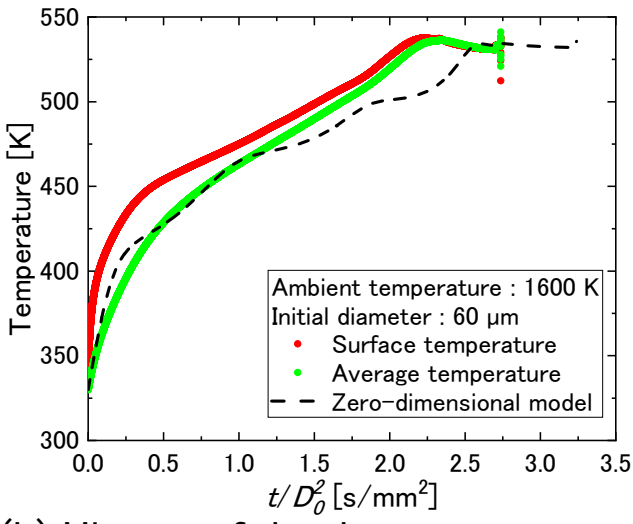

(b) History of droplet temperature

Fig.15 Comparison of the predicted results between the present model and the zero-dimensional model for (a) mass fraction and (b) temperature inside droplet at T_{amb}= 1600 K in D_0=60 μm.

present model and the zero-dimensional model about the history of mass fraction (Fig. 14(a)) and temperature (Fig. 14(b)) inside the droplet at T_{amb} = 600 K in D_0 = 60 μm. According to Fig. 14(a), little differences occur between the history of the mass fraction at the droplet surface and the history of the average mass fraction in all fuel species.

Furthermore, minor differences can be seen for the time histories of mass fraction obtained using the present model and the zero-dimensional model. Figure 14(b) shows little difference between the surface temperature and the average temperature. Additionally, the difference between the history of the droplet temperature between the present model and the zero-dimensional model is insignificant, indicating that the effect of considering internal distribution on the droplet lifetime diminishes at low ambient temperature. On the other hand, Fig. 15 shows the comparison of the predicted results between the present model and the zero-dimensional model regarding the history of mass fraction (Fig. 15(a)) and temperature (Fig. 15(b)) inside the droplet at T_{amb} = 1600 K in D_0 = 60 μm. Fig. 15(a) shows that the differences in the time history between the mass fraction at the droplet surface and the average mass fraction at T_{amb} = 1600 K are larger than those at T_{amb} = 600 K shown in Fig. 14-(a). Furthermore, the differences in the history of mass fraction between the present model and the zero-dimensional model at T_{amb} = 1600 K are also larger than those at T_{amb}=600 K. Fig. 15-(b) shows a large difference between the surface temperature and the average temperature, especially from the early evaporation stage to the middle evaporation stage. Furthermore, the difference between the average droplet temperature given by the present model and the droplet temperature given by the zero-dimensional model is large. This explains why the differences in the droplet lifetime become larger as the ambient temperature increases. Note that the average mass fraction of $C_{20}H_{42}$ suddenly decrease or that of $C_{16}H_{34}$ suddenly increase at the end of the evaporation process, as shown in Fig. 14(a) and Fig. 15(a). This is because the reduction in the effective mass diffusion coefficient ($D_{eff,i}$) given by Eq. (19) due to the reduction in Re_l at the end of the evaporation process leads to a steeper gradient inside the droplet. However, the effect of the increase or decrease in

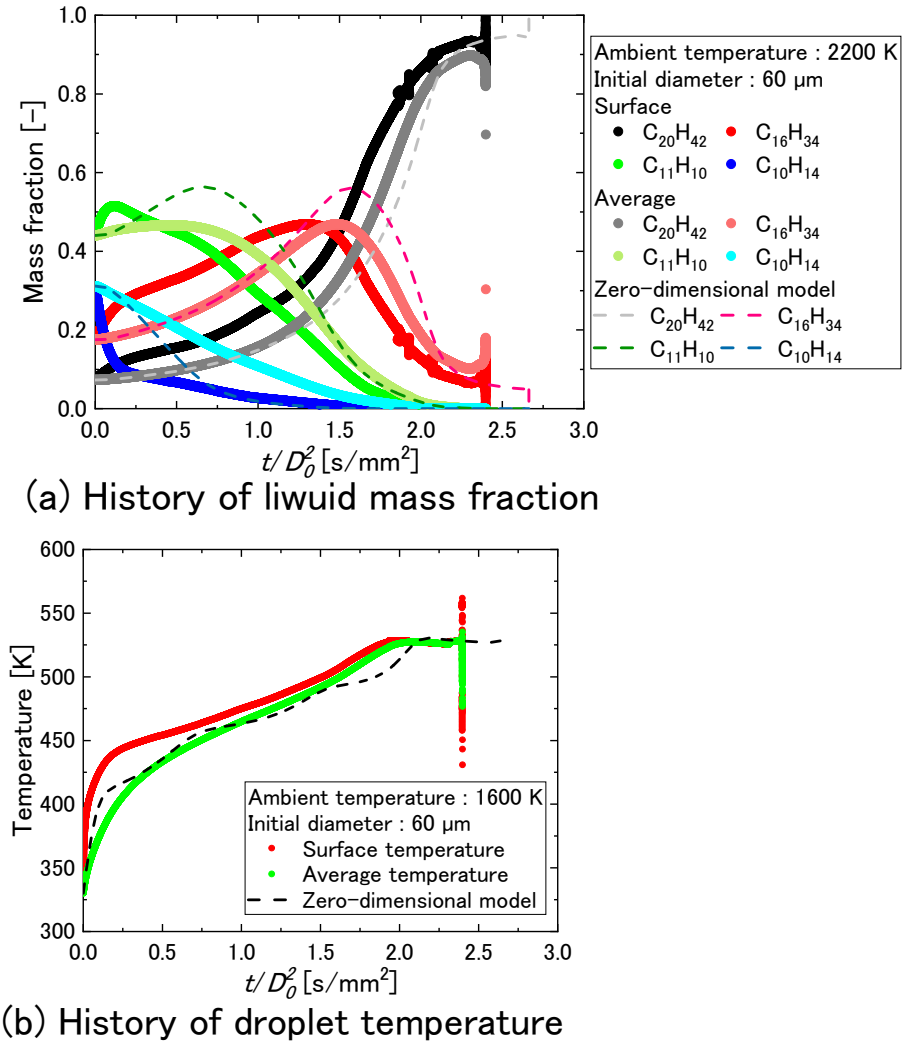

Fig.16 Comparison of the predicted results between the present model and the zero-dimensional model regarding (a) mass fraction and (b) temperature inside droplet at T_{amb} = 2200 K in D_0 = 60 μm.

the average mass fractions at the end of the evaporation process is insignificant.

According to Fig. 13, the difference in the droplet lifetime between the present model and the zero-dimensional model starts to decrease at higher ambient temperatures. In D_0 = 60 μm, the difference in the droplet lifetime between the present model and the zero-dimensional model decreases from T_{amb} = 1600 K to T_{amb} = 2200 K. Fig. 16 shows the comparison of the predicted results between the present model and the zero-

dimensional model regarding mass fraction and temperature inside the droplet at T_{amb} = 2200 K for D_0 = 60 μm. According to Fig. 16(a), the differences in the droplet surface mass fraction between the present model and the zero-dimensional model become small, especially for $C_{20}H_{42}$ and $C_{16}H_{34}$ at the late stage of the evaporation process. Figure 16(b) also shows the small difference between the average droplet temperature given by the present model and the droplet temperature given by the zero-dimensional model.

To explain that the difference in the droplet lifetime between the present model and the zero-dimensional model decreases from T_{amb} = 1600 K to T_{amb} = 2200 K shown in Fig. 13, Figure 17(a) shows the history of the difference in surface mass fraction for $C_{20}H_{42}$ and $C_{16}H_{34}$ between the present model and the zero-dimensional model. Note that the vertical axis shows the absolute value of the differences between the surface mass fraction shown in Fig. 15(a) and that shown in Fig. 16(a). The horizontal axis shows the time normalized by the end time of droplet evaporation term given by the present study ($\tau_{end,present\ model}$). According to Fig. 17(a), the differences between the absolute values at T_{amb} = 1600 K and that at T_{amb} = 2200 K are small from $t/\tau_{end,present\ model}$ = 0–0.7 for both $C_{20}H_{42}$ and $C_{16}H_{34}$. However, the differences at T_{amb} = 2200 K become smaller

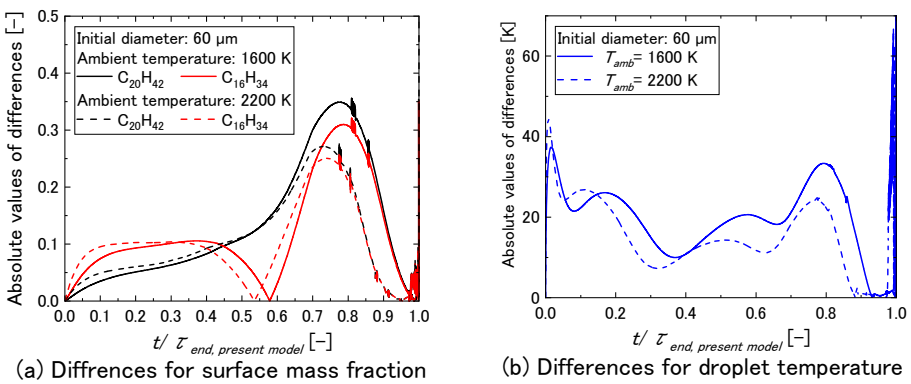

Fig. 17 Comparison of the predicted results between the present model and the zero-dimensional model regarding (a) mass fraction and (b) temperature at the droplet surface

than the differences at T_{amb}= 1600 K from $t/\tau_{end,present\ model}$ = 0.7–1.0. Furthermore, the difference in the surface temperature between the present model and the zero-dimensional model at T_{amb} = 1600 K becomes larger than that at T_{amb} = 2200 K from $t/\tau_{end,present\ model}$ = 0.15–1.0. Consequently, the differences in the droplet lifetime between the present model and the zero-dimensional model decrease from T_{amb} = 1600 –2200 K as shown in Fig.13.

Figure 18 shows the history of the boundary x as a function of dimensionless time normalized by the end of the droplet evaporation term (τ_{end}). The boundary x between the uniform and gradient distributions is defined by the mass diffusion distance from the droplet surface. The mass diffusion distance is determined by the ratio of the effective mass diffusion coefficient $D_{eff,i}$ and the radius regression rate $\dot{R}_d$. Therefore, the boundary is given by $x = R_d - max\ \{D_{eff,i}|i \in N_l\}/\dot{R}_d$. According to Fig. 18, the dimensionless boundary x/R_d approaches to unity over time in all ambient temperatures. This means that the boundary x moves to the droplet surface with time. Furthermore, the boundary x/R_d quickly rises to be close to unity as the ambient temperature increases. According discussed in the previous paragraph, it is expected that the behavior of the boundary x approaching to the droplet surface has two different effects on the evaporation characteristics. First, the

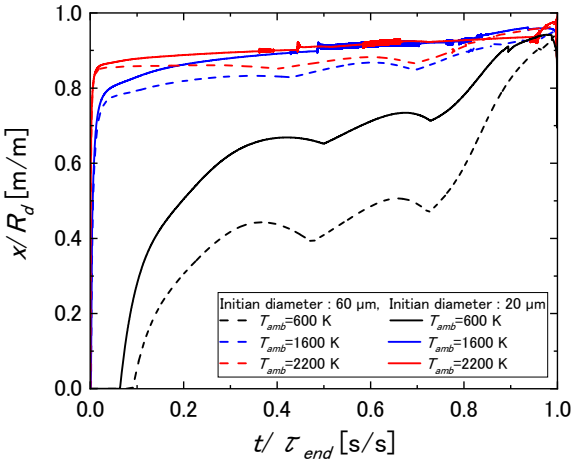

Fig.18 Behavior of the boundary between uniform and gradient distributions under various conditions

gradient distributions inside the droplet become steep because the area forming the gradient distributions becomes narrow. This is why the difference in the droplet lifetime between the present model and the zero-dimensional model increases from T_{amb} = 600 K to T_{amb} = 1600 K. Second, the overall distributions inside the droplet become closer to being uniform because the area of forming the gradient distributions becomes narrow. Thus, the difference in the droplet lifetime between the present model and the zero-dimensional model decreases from T_{amb} = 1600–2200 K.

Additionally, Fig. 13 shows that the difference in the droplet lifetime between the present model and the zero-dimensional model decreases for $D_0 = 20$ μm compared with that for $D_0 = 60$ μm as the ambient temperature increases. According to Fig. 18, the history of the boundary x/R_d for $D_0 = 20$ μm becomes close to the uniform distribution faster than that for $D_0 = 60$ μm in all ambient temperatures. Hence, the differences in the droplet lifetimes between the present model and the zero-dimensional model start to decrease faster than those for $D_0 = 60$ μm. This is why the maximum difference in the droplet lifetime between the present model and the zero-dimensional model for $D_0 = 20$ μm appears at T_{amb} = 1400 K, which is smaller than that for $D_0 = 60$ μm, as shown in Fig. 13.

4. Conclusions

In this study, a droplet evaporation model was developed for multicomponent fuels by considering internal mass fraction and temperature distributions. Our model considers the volume-average mass, $y_{i,l}^{a} \int_0^{R_d} 4\pi R^2\, dR = \int_0^{R_d} y_{i,l}(t,R) 4\pi R^2\, dR$, and enthalpy, $T^a \int_0^{R_d} 4\pi C_{p,l} R^2\, dR = \int_0^{R_d} T(R,t) 4\pi C_{p,l} R^2\, dR$, to simulate the mass and enthalpy

conservation inside the droplet during droplet evaporation process. Additionally, the simulated results were compared with the experimental results at various ambient temperatures to verify the accuracy of the developed model. The main findings are summarized as follows:

1. The internal gradients of both the mass concentration of fuel species and temperature distributions become steeper at higher ambient temperatures. Mass distributions inside the droplet play an important role in droplet evaporation modeling for a multi-component fuel at high ambient temperatures.
2. The droplet lifetimes predicted by the developed model were compared with the experimental results. The droplet lifetimes predicted by the model without the pre-evaporation consideration differed from those measured by the experiment at various ambient temperatures because of the influence of pre-evaporation in the experiments. The droplet lifetimes predicted by the model with the pre-evaporation consideration were in good agreement with the measured droplet lifetimes at various ambient temperatures.
3. The difference in the droplet lifetime between the present model and the zero-dimensional model, which assumes uniform temperature and mass fraction distributions inside the droplet, is more than 10% at various practical spray combustion conditions.

Acknowledgment

This work was partly supported by the Asahi Glass Foundation, Tonen General Sekiyu Research / Development Encouragement & Scholarship Foundation, the MEXT Doctoral program for Data-Related InnoVation Expert Hokkaido University (D-DRIVE-HU)

program, and the f^3 Engineering program in f^3 Engineering Education and Research Center, faculty of Engineering, Hokkaido University.

Appendix A. Physical properties of the liquid phase

The liquid thermal conductivity of hydrocarbons is approximated as

$$k_{i,l} = 10^{\left(A_i + B_i\left(1.0 - \frac{T^a}{T_{i,c}}\right)^{\frac{2}{7}}\right)}$$

where, $\begin{cases} A_i = 0.002911 \times n_i^2 - 0.07139 \times n_i - 1.319595 \\ B_i = -0.002498 \times n_i^2 + 0.05872 \times n_i + 0.710698 \end{cases}$, and $T_{i,c}$ and n_i are the critical temperature [K] and the carbon number of species *i,* respectively. This approximation is reasonable for the hydrocarbons with $5 \leq n_i \leq 25$. The mixed liquid thermal conductivity k_l is given by Pawer Law method [26]:

$$k_l = \left(\sum_{i=1}^{N_l} \frac{y_{i,l}^a}{k_{i,l}^2}\right)^{-0.5}$$

The diffusion coefficient $D_{i,l}(= D_{i,m})$ [m^2/s] can be given by the expansion of the binary diffusion coefficient to the multi-component system by using the methos developed by Perkins and Geankoplis *et.al.* [26]:

$$D_{i,m}\eta_m^{0.8} = \sum_{\substack{j=1 \\ j \neq i}}^{N_l} x_{j,l}^a D_{ij,b}\eta_j^{0.8}$$

where the binary diffusion coefficient $D_{ij,b}$[m^2/s] is given by Hanyduk and Minhas *et.al.* [26]:

$$D_{ij,b} = 8.93 \times 10^{-8} \frac{V_j^{0.267}}{V_i^{0.435}} (\frac{T^a}{\eta_{j,l}})$$

The viscosity of the liquid mixture η_m [kg/m/s] can be given by the expansion of the viscosity of species *i* $\eta_{i,l}$ [kg/m/s] to the multi-component system using the Grunberg and Nissan method.

$$\eta_m = \sum x_{i,l}^a ln\,(\eta_{i,l})$$

where the viscosity of species *i* $\eta_{i,l}$ [kg/m/s] can be estimated by the method developed by Orrick and Erbar *et.al.* [26] method as

$$ln\left(\frac{\eta_{i,l}}{\rho_{i,l} MW_i}\right) = A_i + \frac{B_i}{T^a}$$

where A_i and B_i are the molecular structure-dependent coefficient, $\rho_{i,l}$ is the liquid density of species *i* [kg/m^3], MW_i is the molecular weight [g/mol], T^a is the average temperature inside the droplet [K].

The liquid density of species *i* can be given by

$$\rho_{i,l} = a_i b_i^{\left(-\left(1-\frac{T^a}{T_{i,c}}\right)\right)^{n_i}}$$

The liquid heat capacity of species *i* $C_{i,pl}$ [J/kg/K] can be given using the Ruzika and Domalski method [26].

$$C_{i,pl} = R\left[\sum_{i=1}^{k} n_i a_i + \sum_{i=1}^{k} n_i b_i \frac{T^a}{100} + \sum_{i=1}^{k} n_i d_i \left(\frac{T^a}{100}\right)^2\right]$$

where $n_i a_i, n_i b_i,$ and $n_i d_i$ are the coefficients calculated from molecular structures. The average heat capacity of droplet $C_{p,l}$ can be calculated by $C_{p,l} = \sum y_{i,l}^a C_{i,pl}$. The values

used in this study are shown in Table A.1.

Table A.1 List of coefficients for physical property estimation in the liquid phase

Component		n-eicosane	n-hexadecane	1-methylnaphphalene	tert-butylbenzene
thermal conductivity	n_i	20.000	16.000	11.000	10.000
liquid viscosity	A_i	−11.150	−10.310	−7.1600	−8.7800
	B_i	2255.0	1859.0	414.00	992.00
liquid density	a_i	0.23759	0.24348	0.27189	0.27832
	b_i	0.24934	0.25442	0.22408	0.26103
	n_i	0.30880	0.32380	0.25709	0.28570
liquid heat capacity	$n_i a_i$	58.040	46.851	14.064	21.412
	$n_i b_i$	−1.6693	−1.4495	3.4380	−0.9781
	$n_i d_i$	2.3120	1.8848	0.3056	1.1408

Appendix B. Thermodynamic properties of the gas phase

The thermal conductivity for nitrogen gas k_g [W/m/K] can be estimated by

$$k_g = \frac{252 \times 10^{-5} \times T_{ref}^{1.5}}{T_{ref} + 200}$$

where T_{ref} is the reference temperature [K].

The diffusion coefficient of the gas phase $D_{i,g}$[m^2/s] can be given by the expansion of the binary diffusion coefficient to the multi-component system using Blanc's law .[26].

$$D_{i,g} = \left(\sum_{\substack{j=1 \\ j \neq i}}^{N} \frac{x_{j,g}^{s}}{D_{ij,g}} \right)^{-1}$$

The binary diffusion coefficient of the gas phase $D_{ij,g}$[m^2/s] is given by the method

reported by Reid *et.al.* [26]:

$$D_{ij,g} = \frac{0.0266 T_{ref}^{1.5}}{P_{amb} MW_{ij} \sigma_{ij}^2 \Omega_D}$$

where, $MW_{i,j} = 2\left[\left(\frac{1}{MW_i}\right) + \left(\frac{1}{MW_j}\right)\right]^{-1}$, $\sigma_{i,j} = \frac{\sigma_i + \sigma_j}{2}$

$$\Omega_D = \frac{A}{(T^*)^B} + \frac{C}{exp\,(DT^*)} + \frac{E}{exp\,(FT^*)} + \frac{G}{exp\,(HT^*)}$$

$$\begin{pmatrix} T^* = \frac{k_B T_{ref}}{\sqrt{\varepsilon_A \varepsilon_B}} \\ A = 1.06036, \quad B = 0.15610 \\ C = 0.19300, \quad D = 0.48635 \\ E = 1.03587, \quad F = 1.52996 \\ G = 1.76474, \quad H = 3.89411 \end{pmatrix}$$

The viscosity of the nitrogen gas mixture μ_g [kg/m/s] can be estimated by

$$\mu_g = \frac{1457 \times 10^{-9} \times T_{ref}^{1.5}}{T_{ref} + 110}$$

where T_{ref} is the reference temperature [K].

The density of the gas mixture of the ambient gas (N_2) and fuel vapor ρ_g [kg/m^3]can be calculated using the equation of state for an ideal gas as

$$\rho_g = \frac{\sum_{i=1}^{N} x_{i,ref} MW_i}{\sum_{i=1}^{N} x_{i,ref}} \left(\frac{P_{amb}}{RT_{ref}}\right)$$

The heat capacity for the nitrogen gas mixture $C_{ip,g}$ [J/mol/K] can be calculated as a function of T_{ref}

$$C_{ip,g}(T_{ref}) = R(a_{i,1} + a_{i,2} T_{ref} + a_{i,3} T_{ref}^2 + a_{i,4} T_{ref}^3 + a_{i,5} T_{ref}^4)$$

where R is the universal gas constant and $a_{i,1}, a_{i,2}, a_{i,3}, a_{i,4}$, and $a_{i,5}$ are the coefficients of the fitting function.

The sensible enthalpy of the ambient gas and fuel vapor $h_{i,g}$ [J/mol] can be calculated

by.

$$h_{i,g}(T_{ref}) = \int_0^{T_{ref}} C_{ip,g}(T)dT$$

$$= R(a_{i,1}T_{ref} + \frac{a_{i,2}T_{ref}^2}{2} + \frac{a_{i,3}T_{ref}^3}{3} + \frac{a_{i,4}T_{ref}^4}{4} + \frac{a_{i,5}T_{ref}^5}{5} + a_{i,6})$$

The thermodynamic properties of the mixture of the ambient gas and fuel vapor around the droplet surface are a function of temperature. However, it is difficult to estimate not only the temperature but also the mass fraction of the gas mixture. For the droplet evaporation model, reference values are used on the basis of one-third law as the follows.

$$\begin{cases} T_{ref} = T^s + \frac{1}{3}(T_{amb} - T^s) \\ y_{i,ref} = y_{i,g}^s + \frac{1}{3}(y_{i,g}^{amb} - y_{i,g}^s) \end{cases}$$

The values used in this study are shown in Table B.1.

Table B.1 List of coefficients for physical property estimation in gas phase

		n-eicosane	n-hexadecane	1-methylnaphphalene	tert-butylbenzene	nitrogen
Gas heat capacity	$a_{i,1}$	−1.8392E+00	−1.4019E+00	−6.9950E+00	−7.7671E+00	3.2987E+00
	$a_{i,2}$	2.2898E-01	1.8328E-01	1.0905E-01	1.2036E-01	1.4082E-03
	$a_{i,3}$	−1.2799E-04	−1.0182E-04	−8.1241E-05	−8.6981E-05	−3.9632E-06
	$a_{i,4}$	2.7278E-08	2.1553E-08	2.4223E-08	2.4680E-08	5.6415E-09
	$a_{i,5}$	5.6826E-24	1.2795E-24	1.0332E-24	1.7691E-24	−2.4449E-12
	$a_{i,4}$	0.0000E+00	0.0000E+00	0.0000E+00	0.0000E+00	−1.0209E+03

Appendix C. Nondimension number

Liquid phase:

Reynold's number: $Re_{i,l} = \frac{\rho_l^a u_r d_r}{\eta_{i,l}}$

Peclet number: $Pe_{i,l} = \frac{\rho_l^a u_r d_r C_{i,pl}}{\lambda_{i,l}}$

Gas phase:

Reynold's number: $Re_g = \frac{\rho_g |u_r - u_d| d_r}{\mu_g}$

Grashof number: $Gr_g = \frac{8 g_0 R_l^3 (T_{anb} - T^a)}{\left(\frac{\mu_g}{\rho_g}\right)^2 T_{anb}}$

Schmidt number: $Sc_{i,g} = \frac{\mu_g}{\rho_g D_{i,g}}$

Prandtl number: $Pr_{i,g} = \frac{\mu_g C_{ip,g}}{k_g}$

Sherwood number [33]:

$$Sh_{i,g} = 2.0009 + 0.514 \left(max \left(Re_g, max\left(Gr_g, 0\right)^{\frac{1}{2}} \right) \right)^{\frac{1}{2}} Sc_{i,g}^{\frac{1}{2}}$$

Nusselt number [33]:

$$Nu_{i,g} = 2.0009 + 0.514 \left(max \left(Re_g, max\left(Gr_g, 0\right)^{\frac{1}{2}} \right) \right)^{\frac{1}{2}} Pr_{i,g}^{\frac{1}{2}}$$

The estimation of $\eta_{i,l}$ is described in Appendix A. The estimation of $C_{ip,g}, D_{i,g}$ and μ_g is described in Appendix B.

Appendix D. Boiling model

This section discusses fuel droplet evaporation model with boiling. In this model, the boiling model will be applied when vapour pressure at droplet surface becomes larger than ambient pressure.

It is very difficult to get the boiling point of multi-component fuel qualitatively. Hence, the boiling model will get an approximate solution as the boiling point of multi-component fuel by using Newton's method. First, when fuel droplet become boiling, the vapor pressure at droplet surface become same with ambient pressure. The following relationship can be given.

$$\sum_{i=1}^{N_l} p_{i,v} x_{i,l}^{s} = P_{amb} \tag{D.1}$$

Substituting Eq.(24) into Eq.(D.1), the vapour pressure can be calculated as a function of boiling point.

$$\sum_{i=1}^{N_l} x_{i,l}^{s} 10^{\left(A_{i,p} - \frac{B_{i,p}}{C_{i,p} + T_b - 273.15}\right)} = P_{amb} \tag{D.2}$$

For Newton's method, the following function is defined.

$$g(T_b) = \sum_{i=1}^{N_l} x_{i,l}^{s} 10^{\left(A_{i,p} - \frac{B_{i,p}}{C_{i,p} + T_b - 273.15}\right)} - P_{amb} \tag{D.3}$$

Hence, convergence calculation for the boiling point of multi-component fuel can be given by the following equation.

$$T_b^{n+1} = T_b^{n} - \frac{g(T_b)}{g'(T_b)}$$
$$\text{Convergence judgement: } \left|\frac{g(T_b)}{g'(T_b)}\right| < 10^{-3} \tag{D.4}$$

When fuel droplet become boiling, it is assumed that the droplet surface temperature (T^s) is replaced as the boiling point (T_b) given by the above calculations, and droplet surface is occupied by fuel vapour ($\sum_{i=1}^{N_l} y_{i,g}^{s} = 1$). According to algorithm of the boiling model,

the procedure 4. ~ 8. described in Section 2.6 will be conducted after the droplet surface temperature is replaced as the boiling point.

Appendix E. Overheating model

When the droplet average temperature becomes larger than the droplet surface temperature (overheating), the present model consider the heat up from inside droplet by using correction factor suggested by Adachi *et.al.* [34]. The following is the calculation procedure.

1. Calculate the difference between the droplet surface temperature and average temperature ($\Delta T = T^a - T^s$).
2. If overheat ($\Delta T \geq 0$) occurs, the enthalpy ($\dot{q}_{liquid}$) heat the droplet from inside droplet as the following.

$$\dot{q}_{liquid} = 4\pi R_l^2 \left(h_{liquid} + \alpha_{sh}\right)\Delta T = 4\pi R_d^2 \left(-\frac{k_{eff} \left.\frac{\partial T_l(r)}{R_l \partial r}\right|_{r=1}}{T^s - T_{amb}} + \alpha_{sh} \right) \Delta T$$

Where the correction factor α_{sh} suggested by Adachi *et.al.* can be given by the followings.

$$\begin{aligned} \alpha_{sh} &= 0.76\Delta T^{0.26} && (0 \leq \Delta T < 5) \\ &= 0.027\Delta T^{2.33} && (5 \leq \Delta T < 25) \\ &= 13.8\Delta T^{0.39} && (25 < \Delta T) \end{aligned}$$

3. The mass evaporation rate of species *i* is decided by proportional distribution in response to a mass fraction.

$$\dot{m}_l = \frac{\dot{q}_{gas} - \dot{q}_{liquid}}{H_{latent}}$$

$$\dot{m}_{i,l} = y_{i,g}^{s} \dot{m}_{l}$$

References

[1] H. Nomura, T. Murakoshi, Y. Suganuma, Y. Ujiie, N. Hashimoto, H. Nishida, Microgravity experiments of fuel droplet evaporation in sub- and supercritical environments, Proc. Combust. Inst. 36 (2017) 2425–2432. https://doi.org/10.1016/j.proci.2016.08.046.

[2] H. Moriai, R. Kurose, H. Watanabe, Y. Yano, F. Akamatsu, S. Komori, Large-Eddy Simulation of Turbulent Spray Combustion in a Subscale Aircraft Jet Engine Combustor—Predictions of NO and Soot Concentrations, J. Eng. Gas Turbines Power. 135 (2013) 091503. https://doi.org/10.1115/1.4024868.

[3] D. Noh, S. Gallot-Lavallée, W.P. Jones, S. Navarro-Martinez, Comparison of droplet evaporation models for a turbulent, non-swirling jet flame with a polydisperse droplet distribution, Combust. Flame. 194 (2018) 135–151. https://doi.org/10.1016/j.combustflame.2018.04.018.

[4] T. Kitano, J. Nishio, R. Kurose, S. Komori, Evaporation and combustion of multicomponent fuel droplets, Combust. Flame. 136 (2014) 551–564. https://doi.org/10.1016/j.fuel.2014.07.045.

[5] H. Watanabe, R. Kurose, M. Hayashi, T. Kitano, S. Komori, Effects of ambient

pressure and precursors on soot formation in spray flames, Adv. Powder Technol. 25 (2014) 1376–1387. https://doi.org/10.1016/J.APT.2014.03.022.

[6] M. Takagi, Y. Imai, Evaluation of Ignitability Index and Effect of Pilot Injection on Ignition Characteristics of Light Cycle Oil, Trans. Soc. Automot. Eng. Japan. 50 (2019) 297–302. https://doi.org/10.11351/jsaeronbun.50.297.

[7] P. Yi, H. Zhang, S. Yang, Evaluation of a non-equilibrium multi-component evaporation model for blended diesel/alcohol droplets, AIAA Scitech 2020 Forum. 1 PartF (2020) 1–8. https://doi.org/10.2514/6.2020-2049.

[8] M.S. Dodd, D. Mohaddes, A. Ferrante, M. Ihme, Analysis of droplet evaporation in isotropic turbulence through droplet-resolved DNS, Int. J. Heat Mass Transf. 172 (2021) 121157. https://doi.org/10.1016/j.ijheatmasstransfer.2021.121157.

[9] D.J. Torres, P.J. O'Rourke, A.A. Amsden, Efficient multicomponent fuel algorithm, Combust. Theory Model. 7 (2003) 67–86. https://doi.org/10.1088/1364-7830/7/1/304.

[10] K. Harstad, J. Bellan, Modeling evaporation of Jet A, JP-7, and RP-1 drops at 1 to 15 bars, Combust. Flame. 137 (2004) 163–177. https://doi.org/10.1016/j.combustflame.2004.01.012.

[11] S.L. Singer, Direct Quadrature Method of Moments with delumping for modeling

multicomponent droplet vaporization, Int. J. Heat Mass Transf. 103 (2016) 940–954. https://doi.org/10.1016/j.ijheatmasstransfer.2016.07.067.

[12] P. Yi, W. Long, M. Jia, J. Tian, B. Li, Development of a quasi-dimensional vaporization model for multi-component fuels focusing on forced convection and high temperature conditions, Int. J. Heat Mass Transf. 97 (2016) 130–145. https://doi.org/10.1016/j.ijheatmasstransfer.2016.01.075.

[13] S.S. Sazhin, A. Elwardany, P.A. Krutitskii, G. Castanet, F. Lemoine, E.M. Sazhina, M.R. Heikal, A simplified model for bi-component droplet heating and evaporation, Int. J. Heat Mass Transf. 53 (2010) 4495–4505. https://doi.org/10.1016/j.ijheatmasstransfer.2010.06.044.

[14] S.S. Sazhin, A.E. Elwardany, P.A. Krutitskii, V. Deprédurand, G. Castanet, F. Lemoine, E.M. Sazhina, M.R. Heikal, Multi-component droplet heating and evaporation: Numerical simulation versus experimental data, Int. J. Therm. Sci. 50 (2011) 1164–1180. https://doi.org/10.1016/j.ijthermalsci.2011.02.020.

[15] S.S. Sazhin, M. Al Qubeissi, R. Nasiri, V.M. Gun'Ko, A.E. Elwardany, F. Lemoine, F. Grisch, M.R. Heikal, A multi-dimensional quasi-discrete model for the analysis of Diesel fuel droplet heating and evaporation, Fuel. 129 (2014) 238–266. https://doi.org/10.1016/j.fuel.2014.03.028.

[16] S.S. Sazhin, M. Al Qubeissi, R. Kolodnytska, A.E. Elwardany, R. Nasiri, M.R. Heikal, Modelling of Biodiesel and Diesel Fuel Droplet Heating and Evaporation, Fuel. 115 (2014) 559–572. https://doi.org/10.1016/j.fuel.2013.07.031.

[17] S.S. Sazhin, O. Rybdylova, C. Crua, M. Heikal, M.A. Ismael, Z. Nissar, A.R.B.A. Aziz, A simple model for puffing/micro-explosions in water-fuel emulsion droplets, Int. J. Heat Mass Transf. 131 (2019) 815–821. https://doi.org/10.1016/j.ijheatmasstransfer.2018.11.065.

[18] S.S. Sazhin, P.A. Krutitskii, W.A. Abdelghaffar, E.M. Sazhina, S. V Mikhalovsky, S.T. Meikle, M.R. Heikal, Transient heating of diesel fuel droplets, Int. J. Heat Mass Transf. 47 (2004) 3327–3340. https://doi.org/10.1016/j.ijheatmasstransfer.2004.01.011.

[19] A. Makino, C.K. Law, On the Controlling Parameter in the Gasification Behavior of Multicomponent Droplets, Combust. Flame. 73 (1988) 331–336.

[20] A.W. Cook, Enthalpy diffusion in multicomponent flows, Phys. Fluids. 21 (2009). https://doi.org/10.1063/1.3139305.

[21] Y. Naito, N. Hashimoto, O. Fujita, Development and Validations of Droplet Evaporation Model for Low Ignitibility Fuel Considering Inner Distributions

under Atmospheric Pressure 2 Numerical methods 3 Verification experiments set-up, in: 12th Asia-Pacific Conf. Combust., 2019: pp. 2–5.

[22] A.S. William, Fluid Dynamics and Transport of Droplets and Sprays, Second Edi, n.d.

[23] B. Abramzon, W.A. Sirignano, Droplet vaporization model for spray combustion calculations, Int. J. Heat Mass Transf. 32 (1989) 1605–1618. https://doi.org/10.1016/0017-9310(89)90043-4.

[24] C. Maqua, G. Castanet, F. Lemoine, Bicomponent droplets evaporation: Temperature measurements and modelling, Fuel. 87 (2008) 2932–2942. https://doi.org/10.1016/j.fuel.2008.04.021.

[25] T. Poinsot, D. Veynante, Theoretical and Nemerical Combustion, Edwards, 2005.

[26] B.E. Poling, J.M. Prausnitz, J.P. O'connell, The Properties of Gases and Liquids, McGraw-Hill, New York, 2001.

[27] Y. Naito, K. Ueda, N. Hashimoto, M. Takagi, S. Kawauchi, Y. Imai, M. Watanabe, T. Hasegawa, T. Hayashi, Y. Suganuma, H. Nomura, O. Fujita, Experimental Study on Evaporation Characteristics of Light Cycle Oil Droplet under Various Ambient Conditions, Energy and Fuels. 35 (2021) 6219–6230. https://doi.org/10.1021/acs.energyfuels.0c04406.

[28] Y. Naito, K. Ueda, L. Alexis, N. Hashimoto, Y. Suganuma, H. Nomura, O. FUJITA, Verification of Multicomponent Fuel Droplet Evaporation model for Kerosene under Various Ambient Temperature, in: Fifty-Sixth Symp. Combust., 2018.

[29] N. Hashimoto, H. Nomura, M. Suzuki, T. Matsumoto, H. Nishida, Y. Ozawa, Evaporation characteristics of a palm methyl ester droplet at high ambient temperatures, Fuel. 143 (2015) 202–210. https://doi.org/10.1016/j.fuel.2014.11.057.

[30] Y. Fan, N. Hashimoto, H. Nishida, Y. Ozawa, Spray characterization of an air-assist pressure-swirl atomizer injecting high-viscosity Jatropha oils, Fuel. 121 (2014) 271–283. https://doi.org/10.1016/j.fuel.2013.12.036.

[31] N. Hashimoto, H. Nishida, Y. Ozawa, Fundamental combustion characteristics of Jatropha oil as alternative fuel for gas turbines, Fuel. 126 (2014) 194–201. https://doi.org/10.1016/j.fuel.2014.02.057.

[32] J. Hayashi, N. Hashimoto, H. Nishida, F. Akamatsu, Soot formation characteristics of palm methyl ester spray flames in counterflow sustained bymethane/air premixed flame, At. Sprays. 27 (2017) 1077–1087. https://doi.org/10.1615/AtomizSpr.2018021075.

[33] M. Kulmala, T. Vesala, J. Schwarz, J. Smolik, Mass transfer from a drop-II. Theoretical analysis of temperature dependent mass flux correlation, Int. J. Heat Mass Transf. 38 (1995) 1705–1708. https://doi.org/10.1016/0017-9310(94)00302-C.

[34] M. Adachi, V.G. McDonell, D. Tanaka, J. Senda, H. Fujimoto, Characterization of Fuel Vapor Concentration Inside a Flash Boiling Spray, SAE International Congress and Exposition : technical paper (1997) 163-169. https://doi.org/10.4271/970871